Thermodynamic and Adsorption Characteristics for Various Adsorbent/ refrigerant Pairs

Rupam, Hasan Tahmid
九州大学大学院総合理工学府環境エネルギー工学専攻

https://hdl.handle.net/2324/3053992

出版情報：Kyushu University, 2019, 修士, 修士
バージョン：
権利関係：

THERMODYNAMIC AND ADSORPTION CHARACTERISTICS FOR ADSORBENT/ REFRIGERANT PAIRS

Dissertation

Tahmid Hasan Rupam

(B.Sc. , DU, Bangladesh)

Department of Energy and Environmental Engineering
Interdisciplinary Graduate School of Engineering Sciences

Kyushu University, Japan
2nd August 2019

THERMODYNAMIC AND ADSORPTION CHARACTERISTICS FOR ADSORBENT/ REFRIGERANT PAIRS

A dissertation submitted in partial fulfilment of the requirements for the award of the degree of

Master of Engineering

By

Tahmid Hasan Rupam

(B.Sc. , DU, Bangladesh)

Supervisor: **Professor Bidyut Baran Saha**

Department of Energy and Environmental Engineering
Interdisciplinary Graduate School of Engineering Sciences
Kyushu University, Japan

2nd August 2019

Summary

In today’s world, the primary concern is the energy consumption. Energy consumption have been increased significantly due to the industrial development, supermarkets, automobiles and household appliances. And day after day this ever growing demand for energy is increasing. However, the total amount of energy in the world is fixed. As a result to compensate for future demands for energy or to sustain in the distant future researchers are trying not only to find new sources of energy but also they are looking for efficient use of existing energy. Yes, it is true that in this modern era of science and technology, we are wasting a lot of energy such as low grade heat. This low grade heat can be integrated to some of the wonders of modern science like adsorption cooling systems. These systems can use low grade heat to produce cooling effect. Choosing the right adsorbent/refrigerant pair is the most important task for the construction of a high performance refrigeration system. This thesis is describing the various experiments and simulations so as to achieve the research objective. The key points by each chapter are given as follows:

Chapter 1 deals with the analyzing different functional carbon based adsorbents with various refrigerants on a thermodynamic perspective. Naturally an adsorbent/refrigerant pair is chosen by its adsorption characteristics such as refrigerant uptake and kinetics. However, considering an adsorption system a pair with good uptake and kinetics is not good enough. The pair should also be thermodynamically suitable for the rigorous design of a practical adsorption chiller. Here in this study the adsorbed phase entropy and enthalpy along with the isosteric heat of adsorption is expressed in terms of uptake. Also T-s mapping is done to investigate the entropy flow. Moreover, the applicability of different pairs was studied for different cooling conditions.

In Chapter 2 the synthesis of a metal organic framework (MOF) for water adsorption is discussed. Here aluminum fumarate metal organic framework was synthesized using a

green technology. After that material characterization was done using XRD and FESEM. Porous properties were measured using N_2 adsorption analysis. The porous properties and water adsorption properties of this synthesized aluminum fumarate MOF was compared with the properties of commercially available one.

Chapter 3 focuses on the works done in a different laboratory which involves surface structure determination of Pd(111) using low energy electron diffraction technique. The surface was cleaned inside an ultra-high vacuum chamber and then auger electron spectroscopy and LEED pattern recording was done. The experimental and theoretical I(E) curves were measured and Pendry reliability's factor constant was found to be 0.14.

In the last part of this thesis there is a general conclusion provided mentioning the highlights of different chapters used to compile this work. Moreover, there is brief discussion is provided for future research.

Acknowledgements

This thesis is an outcome of an exciting journey at Kyushu University, which was made possible by the support, care, advice, supervision, and encouragement from several individuals. It is an extremely pleasant opportunity for me to elicit my heartfelt thanks and gratefulness to all of them.

To begin with, I express my deepest sense of gratitude and indebtedness to my supervisor ***Professor Bidyut Baran Saha*** for his precious guidance and inspiration throughout my master course. Success of this thesis work is due to his astute guidance and timely counsel on prioritizing the tasks. He provided me with a pleasant environment at laboratory and much required liberty to conduct my research work. His friendly demeanor and kind nature made my stay in Japan a thoroughly enjoyable experience. Interactions with him have facilitated broaden my perception in manifold aspects of life. I anticipate continuing these interactions and getting opportunities to work with him in the future as well.

I would like express my gratitude to ***Professor Seigi*** **Mizuno** for giving me an opportunity to do research in his laboratory and support me and taking time to examine the manuscript in spite of his busy academic schedule. I am also very thankful to his PhD student ***Mr. Rezwan Ahmed*** for helping me to understand the experimental apparatus and analyzing techniques.

I am grateful to ***Dr. Kutub Uddin*** and ***Dr. Animesh Pal*** for their valuable assistance and providing me the opportunity to discuss technical results of this work any time.

I am grateful to ***Assoc. Prof. Anutosh Chakraborty*** of Nanyang Technological University, Singapore for his help during the internship and research guidance. Special thanks to ***Mr. Shoji Hirano*** for helping me in various ways during my stay in Japan.

I wish to express my heartfelt indebtedness ***Advanced Graduate Program in Global Strategy for Green Asia (GA), IGSES, Kyushu University*** for providing scholarship and

all other facilities required in this study. I would like to acknowledge ***I^{2}CNER*** in Kyushu University for the access of their experimental facilities. I am also grateful to all ***staff of Green Asia*** and ***IGSES staff*** for supporting me in various way during my stay in Kyushu University. I consider myself fortunate to have enjoyed the opportunity of working in Kyushu University under supervision of honorable ***Professor Bidyut Baran Saha***.

I am thankful to all of my present and former laboratory members and staff for their help and kind cooperation. In particular, I must thank to ***Mr. Amirul Islam, Mr. M L Palash, Mr. Mahbubul Muttakin, , Mr. Mohamed Younes, Mr. Sampad Ghosh, Mr. Kaiser Ahmed Rocky, Mr. Matiar Rahman, Ms. Yang Jiahui, Ms. Mahua Jahan Alam,*** **Ms. Jahan Israt, Mr.** ***Perera Colombatantirige Uthpala Amoda, Ms.Bai Yibing, Mr. Karmaker Shamal Chandra, Mr. Islam Mir Shariful*** ,for making me feel comfortable in the lab and for supporting me in various ways.

I would also like to special thanks to ***Mrs. Tandra Bhuiyan Saha***, wife of my supervisor, for giving advice, suggestions and taking care during my stay in Japan. Because of her wise suggestions, my Japan life was very smooth, funny and enjoyable. Thank you very much for the quality times.

I express my humble obligation to my affectionate and loving Father, Mother, Brother, and In-Laws for their love, inspiration and prayers for me. In particular, I am thankful and would like to express my gratitude to my father ***MD Belayet Hossain***, mother ***Tahmina Akhter*** and my younger brother ***Tahjib Hasan Rhythm*** for everything they have done for me.

Finally, I wish to thank my beloved wife ***Farhana Jesmin Tuli*** for the understanding, quiet patience and encouragement during my study.

Tahmid Hasan Rupam

Kyushu University, Japan

CONTENTS

Chapter 3. Optimizing pore size distribution of activated carbon for adsorptive heat pump by selective removal of unusable pores ………………..... **42**

LIST OF FIGURES

LIST OF TABLES

CHAPTER 1

Thermodynamic property surfaces for various adsorbent/adsorbate pairs for cooling application

CHAPTER 1

Thermodynamic property surfaces for various adsorbent/adsorbate pairs for cooling application

This study focuses on comparative analysis of five different adsorbent/adsorbate pairs regarding thermodynamic property fields based on some well-established mathematical modelling. The thermodynamic property fields - enthalpy (*h*), entropy (*s*) are expressed in terms of temperature, pressure and adsorbed quantity. Moreover, the isosteric heat of adsorption for pairs having a common adsorbent with the three different refrigerants were compared to investigate the effect of adsorbate molecules on the isosteric heat of adsorption. T-s diagrams are analyzed for all the five pairs for different cooling conditions- 5 °C, 10 °C and 15 °C. This information along with the isotherms and kinetics data find immense importance in the computation of energy balances of the adsorbed phase. These results are crucial for rigorous design and analysis of adsorption cooling systems.

Keywords

D-A modelling; enthalpy; entropy; heat of adsorption; Maxsorb III.

Nomenclature

c	specific heat capacity [J kg^{-1} K^{-1}]
E	activation energy [J kg^{-1}]
h	enthalpy [J kg^{-1}]
H_{ads}	isosteric heat [J kg^{-1}]
m	mass [kg]
M	adsorbent mass [kg]
n	fitting parameter [-]
P	pressure [Pa]
q	instantaneous uptake [kg kg^{-1}]
q^*	maximum uptake [kg kg^{-1}]
R	molar gas constant [J kg^{-1} K^{-1}]
s	specific entropy [J K^{-1} kg^{-1}]
S	entropy [J K^{-1}]
v	specific volume [m^3 kg^{-1}]
V	volume [m^3]

Greek letters

Δ	difference [-]
μ	chemical potential [J kg^{-1}]

Subscript

a	adsorbate
ad	adsorbent
ads	adsorbed phase
cond	condenser
des	desorbed phase
evap	evaporator
f	fluid

g	gas

Acronyms

CFCs	chlorofluoro-carbons
GWP	global warming potential
HCs	hydro-carbons
HFCs	hydrofluoro-carbons
HCFCs	hydro-chloro-fluoro-carbons
HFOs	hydrofluro-olefins
ODP	ozone depletion potential
UNFCCC	united nations framework convention on climate change
UNEP	united nations environment programme

1.1 INTRODUCTION

Gas or vapour adsorption finds its immense importance in the fields of gas separation [1–3], gas purification[4,5], adsorption chillers [6–8], cryocoolers [9] and energy storage systems [10]. In solid-gas physical adsorption, over a wide range of temperature and pressure, gas molecules come into contact with a porous solid adsorbent and impinge against the surface behaving non-ideally as some molecules are captured by the Van der Waals forces created from the dangling bonds in the surface atoms while the uncaptured molecules depart. When the surface forces are relatively intense resulting in molecules leaving the adsorbent surface being negligible, the gas molecules will form a layer covering the surface of the porous adsorbent. However, there can be other uses of adsorption such as pollutants removal from the environment such as heavy metal ions [11], organic dyes [12,13], oils, and other contaminants [14,15]. Physical adsorption mainly occurs within the pores of adsorbent and the exterior surface of the adsorbents. To understand this phenomena, the knowledge of adsorption characteristics over a wide range of temperature and pressure are required [16]. Adsorption isotherms and porous property determination are the traditional ways of characterising a single component adsorbent/adsorbate system. Numerous studies have been conducted on synthesising different adsorbents [17,18]. Researchers also modified the commercially available parent adsorbents using different treatments [19,20]. All these adsorbents had been characterised using the traditional methods with various adsorbates (both natural and commercial) [6,21–24]. However, this characterisation is incomplete without the thermodynamic properties such as entropy, enthalpy and isosteric heat of adsorption. This additional information is required for analysing and development of a practical adsorption bed. Hence some research works involve thermodynamic analysis along with the porous properties and adsorption isotherms [16,25–27]. However, there is hardly any literature which compares different adsorbent/adsorbate pairs in terms of their thermodynamic property fields.

Among a wide-ranging choice of adsorbents, activated carbons (AC) are most popular for their high adsorption capacity, faster kinetics, high surface area, uniform pore size distribution and thermal stability. Moreover, they are inexpensive and insensitive to moisture. [28] There are many types of activated carbons commercially available such as - Maxsorb III, surface treated activated carbons, biomass derived activated carbons, activated carbon fiber (ACF) and so forth. In this study Maxsorb III and ACF-A20 were chosen as adsorbents. The SEM image of these two are shown in Figure 1.1 (a) and (b). A lot of studies so far has been done on these adsorbents using various adsorbates [8,29–32]. The porous properties of these two adsorbents are presented in Table 1.1.

Table 1.1 Porous properties of the assorted adsorbents.

Adsorbent	BET surface area [m^2/g]	Total-pore volume [ml/g]	Average pore width [nm]	Reference
Maxsorb III	3150	2.01	2.008	[27]
ACF-A20	1930	1.028	2.160	[8]

In case of refrigerant selection, the choice was not so straightforward. In the early stages there were few choices of refrigerants. People did not care about toxicity, flammability, environmental impacts, high pressure hazards during selection of refrigerants. They used whatever worked as refrigerants [33]. With the continuous development of refrigeration technology, many new refrigerants such as - CFCs, HCFCs, HFCs, HCs, HFOs have emerged with their pros and cons. CFCs and HCFCs had chlorine in their structure which acted as a potential threat for ozone layer depletion. These refrigerants either have phased out or in the verge of being phased out because of the actions of different international organizations such as – UNFCCC (United Nations Framework Convention on Climate Change), UNEP (United Nations Environment Programme), etc. Several protocols and amendment took place after the Vienna Convention in controlling these hazardous refrigerants [34–36]. Hence, now a days HFCs and HCs have been preferred as refrigerants. Although, HFCs and HCs have zero ozone depletion potential (ODP), HFCs are potential candidate for global warming and HCs are flammable. Concerning these factors, the refrigerants preferred in this study – n-butane, R134a and R32 and their properties are shown in table 1.2. Figure 1.1 (c) illustrates the molecular structures of the assorted refrigerants.

Table 1.2 Properties of the selected refrigerants [37–44].

Refrigerants	**R600**	**R134a**	**R32**
Chemical formula	C_4H_{10}	$C_2H_2F_4$	CH_2F_2
Chemical name	n-butane	Tetrafluoroethene	Difluoromethane
ODP	0	0	0
GWP	4	1300	675
Normal boiling Point (°C)	-0.50	-26.07	-51.5
Critical temperature (°C)	152	101.1	78.26
Critical pressure (MPa)	3.79	4.05	5.78
Toxicity	No	No	No
ASHRAE safety group	A3	A1	A2L

This study focuses on five different functional pairs: ACF-A20/R32 [45], Maxsorb III/n-butane [27], ACF-A20/R134a [22], MAXSORB III/R32 [45] and Maxsorb III/R134a [32] to express their thermodynamic property fields in terms of isosteric heat, temperature, pressure and amount of adsorbate and provide a comparative analysis among them in thermodynamic viewpoint, intended for practical adsorption chiller applications. Furthermore, to investigate the effect of refrigerant's physical properties on the heat of adsorption; the heat of adsorption of Maxsorb III/R32 [45] and Maxsorb III/R134a [32] pairs were compared with Maxsorb III/n-butane pair.

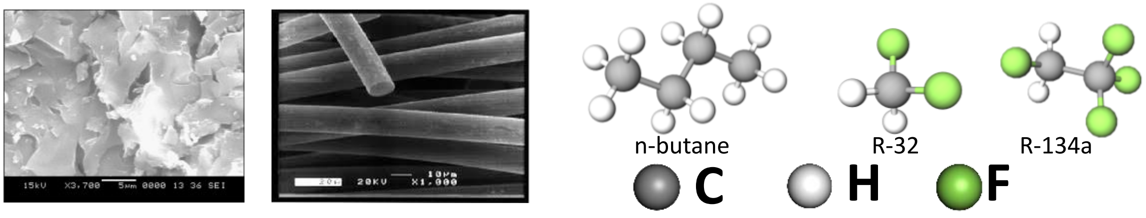

(a) (b) (c)

Figure 1.1 (a) SEM image of Maxsorb III [27], *(b) SEM image of ACF-A20* [46] *(c) molecular structures of refrigerants.*

Adsorption isotherms for all the mentioned pairs have been fitted with D-A modelling in the literature. Table 1.3 indicates the values of adjustable parameters for best fitting.

Table 1.3 Adjustable parameters for D-A isotherm modelling of different adsorbent-adsorbate pairs.

Adsorption pairs	**n** **[-]**	**q*** **[kg kg^{-1}]**	**E** **[kJ kg^{-1}]**	**Error**
ACF-A20/R32[45]	1.09	1.014	104	AAD 0.005 Kg Kg^{-1}
Maxsorb III/n-butane [27]	1.05	0.8	300	*
ACF-A20/R134a [22]	1.4	1.256	68.6	ARE 3.2%
Maxsorb III/R32 [45]	1.15	1.57	75.72	AAD 0.03 kg kg^{-1}
Maxsorb III/R134a [32]	1.17	1.945	85.27	*

* Not available in the literature

1.2 MATHEMATICAL MODELLING

1.2.1 Isosteric heat of adsorption:

The isosteric heat of adsorption H_{ads} is defined as the differential change in energy δQ that occurs when an infinitesimal amount of adsorbate uptake δq is transferred at constant pressure P, temperature T, and the amount of adsorbent M_s or the constant adsorbent surface ranging from the bulk gas phase to the adsorbed phase [47].

$$\Delta H_{ads} = \left(\frac{\partial Q}{\partial q}\right)_{P,T,M_s} \tag{1}$$

According to the mass balance, the number of molecules adsorbed (m_a) in the adsorbent must be equal to the number of molecules lost from the adsorbate (m_g).

$$dm_a = -dm_g \Rightarrow d\left(\frac{m_a}{M_s}\right) = -d\left(\frac{m_g}{M_s}\right) \Rightarrow dq = -d\left(\frac{m_g}{M_s}\right) \tag{2}$$

Here, q is the uptake term having a unit of kg kg^{-1}. The elemental heat rejected on to the adsorbent can be found using the 2nd law of thermodynamics as-

$$-dQ = TdS \tag{3}$$

Where S is the sum of entropy changes in the system. S is expressed as-

$$S = S_s + S_a + S_g \tag{4}$$

Where s, a, and g denote solid, adsorbed and gaseous phase. Substituting the values from equations (3) and (4) into equation (1) the isosteric heat of adsorption takes the form as -

$$\Delta H_{ads} = -T\left[\left(\frac{\partial S_s}{\partial q}\right)_{P,T,M_s} + \left(\frac{\partial S_a}{\partial q}\right)_{P,T,M_s} + \left(\frac{\partial S_g}{\partial q}\right)_{P,T,M_s}\right] \tag{5}$$

As $\left(\frac{\partial S_s}{\partial q}\right)_{P,T,M_s} \approx 0$, equation (5) can be written as,

$$\Delta H_{ads} = -T\left[\left(\frac{\partial S_a}{\partial q}\right)_{P,T,m_s} - s_g\right] \tag{6}$$

Now, the chemical potential of the adsorbed phase is a result of the partial change in internal energy (u) with the amount of adsorbate uptake (q) [25].

$$\mu_a \left[= \left(\frac{\partial u}{\partial q} \right)_{s,v,\mu_g} \right] \tag{7}$$

Therefore,

$$d\mu_a = -\left(\frac{\partial S_a}{\partial q} \right)_{T,P} dT + \left(\frac{\partial V_a}{\partial q} \right)_{T,P} dP + \left(\frac{\partial \mu_g}{\partial q} \right)_{T,P} dq \tag{8}$$

And similarly for gaseous phase chemical potential,

$$d\mu_g = -s_g dT + v_g dP \tag{9}$$

At equilibrium, $\mu_a \cong \mu_g$. Hence, it can be written as $d\mu_a = d\mu_{g.}$

So combining equations (7) and (8), we get -

$$\left(\frac{\partial S_a}{\partial q} \right)_{T,P} dT - \left(\frac{\partial V_a}{\partial q} \right)_{T,P} dP - \left(\frac{\partial \mu_g}{\partial q} \right)_{T,P} dq = s_g dT - v_g dP \tag{10}$$

For a constant amount of adsorbate,

$$\left(\frac{\partial \mu_g}{\partial q} \right)_{T,P} = 0 \tag{11}$$

From equation (10) -

$$\left(\frac{\partial S_a}{\partial q} \right)_{T,P} dT - s_g dT = v_a dP - v_g dP \tag{12}$$

or,

$$\left(\frac{\partial S_a}{\partial q} \right)_{T,P} = s_g - (v_g - v_a) \frac{dP}{dT} \tag{13}$$

Using equation (13) in equation (6), the isosteric heat of adsorption can be expressed as,

$$\Delta H_{ads} = -T[v_g - v_a] \frac{dP}{dT} \tag{14}$$

Where, v_g and v_a are the specific volumes of the gas and the adsorbed phase, respectively.

The pressure of an adsorbed phase is exerted by both the temperature and the uptake, i.e., *P=P(T,q)*.

So the gradient of the adsorbed phase pressure with respect to the temperature can be expressed as -

$$\frac{dP}{dT} = \left(\frac{\partial P}{\partial q}\right)_T \frac{dq}{dT} + \left(\frac{\partial P}{\partial T}\right)_q \tag{15}$$

Thus, the heat of adsorption or isosteric heat of adsorption (H_{ads}) as a function of uptake (q) can be calculated by the following equation.

$$\Delta H_{ads} \cong T v_g \left(\frac{\partial P}{\partial m_a}\right)_T \frac{dm_a}{dT} + RT^2 \left(\left[\frac{\partial(\ln P)}{\partial T}\right]_{m_a}\right) \tag{16}$$

Here, the second term of the right-hand side indicates the conventional form of the isosteric heat of adsorption derived from the Clausius-Clapeyron equation. Besides, the first term defines the behaviour of adsorbed mass concerning both the pressure and the temperature changes during an adsorbate uptake because of the non-ideality of its gaseous phase.

The DA equation for adsorption isotherms can be expressed as follows -

$$q = q_m \exp\left[-\left\{\frac{RT}{E}\ln\left(\frac{P_s}{P}\right)\right\}^n\right] \tag{17}$$

$$\Rightarrow \qquad \ln\left(\frac{q}{q_m}\right) = -\left\{\frac{RT}{E}\ln\left(\frac{p_s}{P}\right)\right\}^n \tag{18}$$

$$\Rightarrow \qquad \ln p = \ln p_s - \frac{E}{RT}\left\{-\ln\left(\frac{q}{q_m}\right)\right\}^{1/n} \tag{19}$$

Differentiating with respect to T yields,

$$\frac{\partial \ln P}{\partial T} = \frac{\partial}{\partial T}\ln(P_s) + \frac{E}{RT^2}\left\{-\ln\left(\frac{q}{q_m}\right)\right\}^{1/n} \tag{20}$$

$$\Rightarrow \qquad RT^2\frac{\partial \ln P}{\partial T} = RT^2\frac{\partial}{\partial T}\ln(P_s) + E\left\{-\ln\left(\frac{q}{q_m}\right)\right\}^{1/n} \tag{21}$$

Now substituting the value of $RT^2 \frac{\partial \ln P}{\partial T}$ in equation (16), we have an expression for the isosteric heat as a function of uptake -

$$\Delta H_{ads} = h_{fg} + E \ln\left(\frac{q^*}{q}\right)^{\frac{1}{n}} + Tv_g \frac{dP}{dT}(P,T) \tag{22}$$

Where, $h_{fg} = RT^2 \frac{\partial}{\partial T} \ln\left(P_{sat}\right)$ (23)

1.2.2 Enthalpy and entropy of adsorption system

In physical adsorption, the thermodynamic properties such as the entropy (s) and enthalpy (h) of the adsorbed phase are described in terms of the measured variables, namely P, T and m_a. The accurate measurement of h and s requires the isosteric heat of adsorption and the specific heat of the adsorbed phase are necessary. Being path independent, the change of extensive thermodynamic quantity can be tracked by taking their integrating form. For example, from-

(i) an initial reference pressure P_0 to non-equilibrium pressure P at constant T and m_a, followed by an initial reference temperature, T_0, to temperature, T, at zero adsorbate ($m_a = 0$), and finally from zero amount of adsorbate to any adsorbate uptake, m_a, at constant T and P,
or (ii) firstly, an initial reference amount of adsorbate uptake (here $x \neq 0$) to an adsorbate uptake, m_a, at constant T and P, then from an initial reference temperature, To, to temperature, T, at constant P and m_a, and finally from zero adsorbate to adsorbate mass, m_a, at constant T and P.

The integration of the thermodynamic properties can also be depicted schematically in Figure 1.2. In the following sections, we approach the properties of the adsorbed phase by first considering the entropy as a function of P, T and m_a. The Gibbs law is then invoked to calculate enthalpy [48].

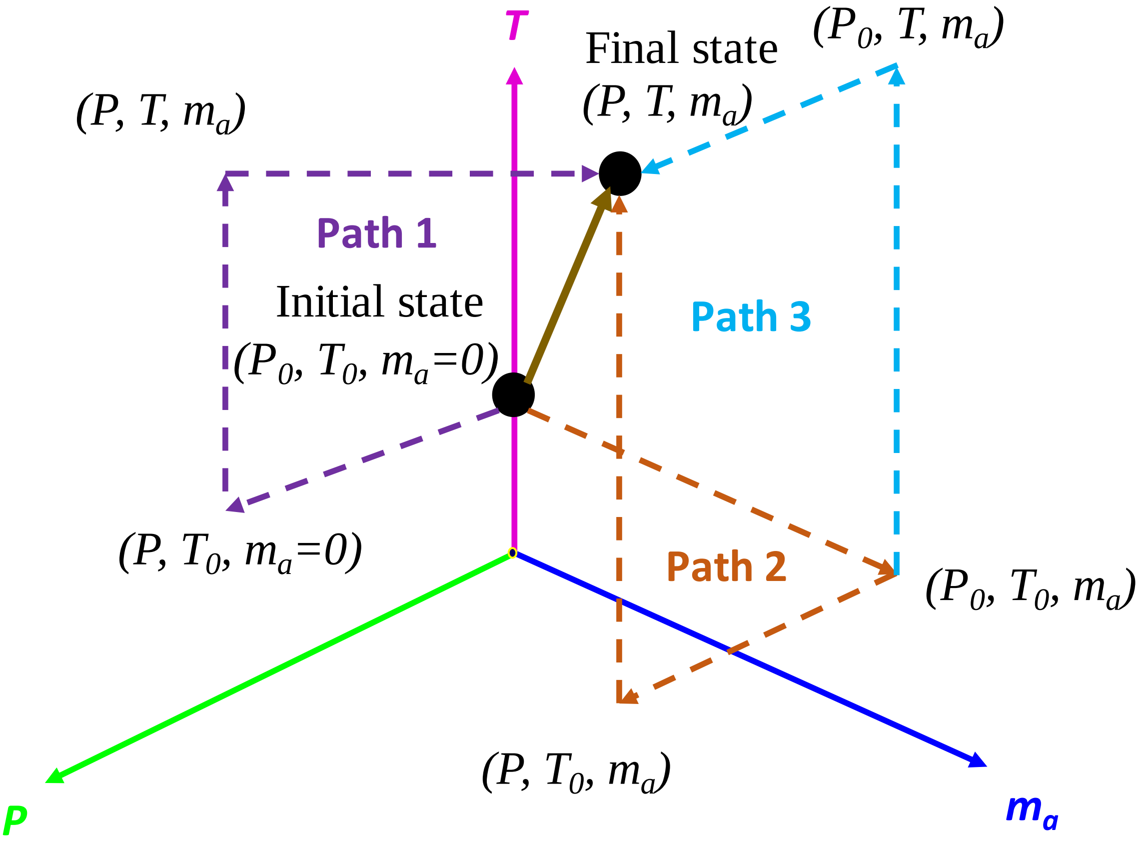

Figure 1.2 Three possible thermodynamic paths for calculating extensive thermodynamic properties from the initial state to final state [48]

The total differential of the extensive thermodynamic property, enthalpy of an adsorbent/adsorbate system can be written as -

$$dh = dh_a + dh_s \tag{24}$$

Where, dh_s are the total differential of the solid phase enthalpy, and dh_a is that of adsorbate phase enthalpy.

Using the relation between derivatives, the total differential of the solid phase enthalpy is written as -

$$dh_s = \left(\frac{\partial h_s}{\partial T}\right)_p dT + \left(\frac{\partial h_s}{\partial P}\right)_T dP = Mc_{p,s}dT + \left\{T\left(\frac{\partial s_s}{\partial P}\right)_T + v_s\right\}dP \tag{25}$$

Using Maxwell's relationship given in equation (26); equation (25) takes the form expressed in equation (27) -

$$\left(\frac{\partial s_s}{\partial P}\right)_T dP = -\left(\frac{\partial v_s}{\partial T}\right)_p dP \tag{26}$$

$$dh_s = Mc_{p,s}dT + \left\{v_s - T\left(\frac{\partial v_s}{\partial T}\right)_p\right\}dP \tag{27}$$

On the other hand, the total differential of the adsorbed phase enthalpy is given by -

$$dh_a = \left(\frac{\partial h_a}{\partial T}\right)_{p,m_a} dT + \left(\frac{\partial h_a}{\partial P}\right)_{T,m_a} dP + \left(\frac{\partial h_a}{\partial m_a}\right)_{T,P} dm_a \tag{28}$$

Using the Gibbs equation, the Maxwell relation, and the relation between derivatives, the first, second and third term of the right-hand side of the above equation can be expressed as -

$$\begin{gathered}\left(\frac{\partial h_a}{\partial T}\right)_{P,m_a} = m_a c_{P,a}\ ;\ \left(\frac{\partial h_a}{\partial P}\right)_{T,m_a} = \left\{T\left(\frac{\partial s_a}{\partial P}\right)_T + v_a\right\}dP = \left\{v_a - T\left(\frac{\partial v_a}{\partial T}\right)_P\right\}dP \\ \text{and}\quad \left(\frac{\partial h_a}{\partial m_a}\right)_{T,P} dm_a = \left(h_g - \Delta H_{ads}\right)dm_a\end{gathered} \tag{29}$$

Now substituting the values of dh_a and dh_s into equation (24), the differential expression for measuring adsorbed phase enthalpy becomes -

$$dh = Mc_{p,s}dT + m_a c_{p,a}dT + \left\{v_s - T\left(\frac{\partial v_s}{\partial T}\right)_P\right\}dP + \left\{v_a - T\left(\frac{\partial v_a}{\partial T}\right)_P\right\}dP + \left(h_g - \Delta H_{ads}\right)dm_a \tag{30}$$

Neglecting the pressure and uptake dependence of solid phase thermodynamic properties with respect to pressure and temperature, the enthalpy of the adsorbent/adsorbate system becomes -

$$h = c_{p,ad}\int_{T_o}^{T} dT + \int_{T_o}^{T}\left[c_{p,g}(P,T) + \frac{\Delta H_{ads}}{T} - \frac{\Delta H_{ads}}{v_g}\frac{\partial v_g}{\partial T} - \frac{\partial \Delta H_{ads}}{\partial T}\right] dT + \int_{0}^{q}\left[h_g(P,T) - \Delta H_{ads}\right] dq + \int_{p_o}^{p} v_{ad}\, dP \tag{31}$$

Where,

$q = \dfrac{m_a}{M}$; $\Delta H_{ads} = -T[v_g - v_a]\dfrac{dP}{dT}$ and $c_{p,a} = c_{P,g} + \dfrac{\Delta H_{ads}}{T} - \dfrac{\Delta H_{ads}}{v_g}\left(\dfrac{\partial v_g}{\partial T}\right)_p - \dfrac{\partial H_{ads}}{\partial T}$ [49].

Again, in the case of entropy, it is measured by the summation of its solid and adsorbed phases.

$$ds = ds_a + ds_s \tag{32}$$

Subscripts ‘s’ and ‘a’ indicate the solid adsorbent and adsorbate, respectively.

The extensive entropy of the solid phase as a function of *P* and *T* is given by-

$$ds_s = \left(\frac{\partial s_s}{\partial T}\right)_p dT + \left(\frac{\partial s_s}{\partial P}\right)_T dP = M\frac{c_{p,s}}{T}dT - \left(\frac{\partial v_s}{\partial T}\right)_p dP \tag{33}$$

And the total differential of entropy in the adsorbed phase is

$$ds_a = \left(\frac{\partial s_a}{\partial T}\right)_{p,m_a} dT + \left(\frac{\partial s_a}{\partial P}\right)_{T,m_a} dP + \left(\frac{\partial s_a}{\partial m_a}\right)_{P,T} dm_a \tag{34}$$

where the first term of the right-hand side refers to the partial change of entropy with respect to temperature at constant pressure and the amount of adsorbate uptake and is written as -

$$\left(\frac{\partial s_a}{\partial T}\right)_{p,m_a} dT \approx m_a\frac{c_{p,a}}{T} \tag{35}$$

The second term represents the change of entropy as a function of pressure at constant temperature and the amount of adsorbate in the adsorbed phase, and, using Maxwell relationship, this can be expressed as -

$$\left(\frac{\partial s_a}{\partial P}\right)_{T,m_a} = -\left(\frac{\partial v_a}{\partial T}\right)_{p,m_a} \tag{36}$$

And the third term $\left(\frac{\partial s_a}{\partial m_a}\right)_{P,T}$ is defined as the change of entropy with respect to the amount of adsorbate.

It is well-known that the chemical potential of an adsorbed phase $\mu_a\left[=\left(\frac{\partial u}{\partial m_a}\right)_{s,v,\mu_g}\right]$ is a result of the partial change in internal energy (u) with the amount of adsorbate uptake (m_a).

Therefore,

$$d\mu_a = -\left(\frac{\partial S_a}{\partial m_a}\right)_{T,P} dT + \left(\frac{\partial V_a}{\partial m_a}\right)_{T,P} dP + \left(\frac{\partial \mu_g}{\partial m_a}\right)_{T,P} dm_a \tag{37}$$

Similarly, for gaseous phase chemical potential,

$$d\mu_a = -\left(\frac{\partial S_g}{\partial m_g}\right)_{T_s,P} dT + \left(\frac{\partial V_g}{\partial m_g}\right)_{T,P} dP \tag{38}$$

At equilibrium, $\mu_a \cong \mu_g$. So, we can write -

$$d\mu_a = d\mu_g$$

$$\Rightarrow \quad \left(\frac{\partial S_a}{\partial m_a}\right)_{T,P} dT - \left(\frac{\partial V_a}{\partial m_a}\right)_{T,P} dP - \left(\frac{\partial \mu_g}{\partial m_a}\right)_{T,P} dm_a = \left(\frac{\partial S_g}{\partial m_g}\right)_{T_s,P} dT - \left(\frac{\partial V_g}{\partial m_g}\right)_{T,P} \tag{39}$$

For a constant amount of adsorbent,

$$\left(\frac{\partial \mu_g}{\partial m_a}\right)_{T,P} = 0 \tag{40}$$

Now we have,

$$\left(\frac{\partial S_a}{\partial m_a}\right)_{T,P} dT - \left(\frac{\partial S_g}{\partial m_g}\right)_{T_s,P} dT = \left(\frac{\partial V_a}{\partial m_a}\right)_{T,P} dP - \left(\frac{\partial V_g}{\partial m_g}\right)_{T,P} dP \tag{41}$$

$$s = \int_{T_o}^{T} \frac{c_{p,s}}{T} dT + \int_{0}^{m_a} \left[s_g - \frac{\Delta H_{ads}}{T} \right] dm_a + q\int_{T_0}^{T} \left[c_{P,g} + \frac{\Delta H_{ads}}{T} - \frac{\Delta H_{ads}}{v_g} \left(\frac{\partial v_g}{\partial T} \right)_p - \frac{\partial H_{ads}}{\partial T} \right] \frac{dT}{T} \quad (42)$$

Or,

$$\left(\frac{\partial S_a}{\partial m_a} \right)_{T,P} = s_g - (v_g - v_a) \frac{dP}{dT} \quad (43)$$

Now, substituting appropriate terms in equations (33) – (35) and combining them, the differential equation for calculating adsorbed phase entropy takes the following form -

$$ds = M \frac{c_{p,s}}{T} dT + m_a \frac{c_{p,a}}{T} dT - \left(\frac{\partial v_s}{\partial T} \right)_p dP - \left(\frac{\partial v_a}{\partial T} \right)_{p,m_a} dP + \left\{ s_g - (v_g - v_a) \frac{dP}{dT} \right\} dm_a \quad (44)$$

After simplification,

$$s = M \int_{T_o}^{T} \frac{c_{p,s}}{T} dT + m_a \int_{T_o}^{T} \frac{c_{p,a}}{T} dT + \int_{0}^{m_a} \left\{ s_g - (v_g - v_a) \frac{dP}{dT} \right\} dm_a \quad (45)$$

Which can be further expressed for per unit mass of the adsorbent (M=1) as,

$$s = \int_{T_o}^{T} \frac{c_{p,s}}{T} dT + q\int_{T_0}^{T} \left(c_{P,g} + \frac{\Delta H_{ads}}{T} - \frac{\Delta H_{ads}}{v_g} \left(\frac{\partial v_g}{\partial T} \right)_p - \frac{\partial H_{ads}}{\partial T} \right) \frac{dT}{T} + \int_{0}^{q} \left\{ s_g - \frac{\Delta H_{ads}}{T} \right\} dq \quad (46)$$

1.3 RESULTS AND DISCUSSION

Equation (22) is used to calculate the isosteric heat data of the studied pairs which are shown in *Figure 1.3*.

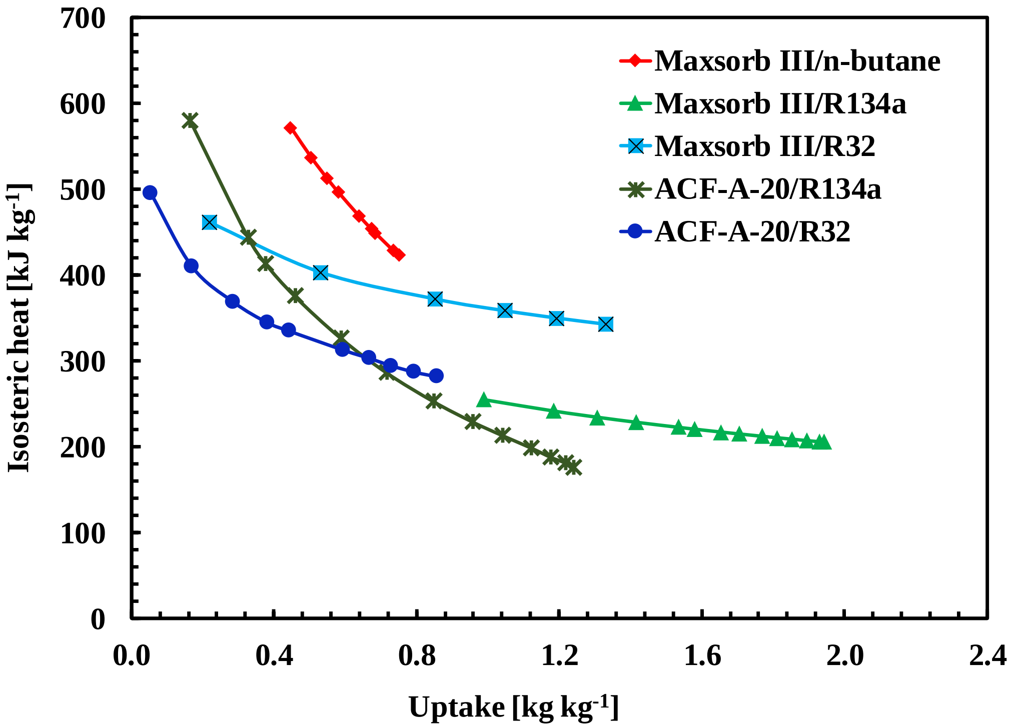

Figure 1.3 Comparison of isosteric heat of adsorption.

It is evident from *Figure 1.3*. that, all the five pairs exhibit a common characteristic – the isosteric heat of adsorption decrease with the increment of surface loading. This happens because the adsorbate is first adsorbed in the narrower pores of the adsorbents. These narrower pores are high in energy and cause a relatively high adsorbate-adsorbent interaction. As a result, the isosteric heat or the heat rejection during adsorption is the highest at the beginning of the adsorption process. After occupying all the high energy sites, the adsorbate molecules enter into the pore sites having less energy which results in a lower isosteric heat. When comparing within the five assorted adsorbent-refrigerant pairs, it can be observed that Maxsorb III/n-butane pair possesses highest isosteric heat at lower uptake values and decreases rapidly with surface coverage. Whereas, the isosteric heat of adsorption decreases slowly for ACF-A20/R32, Maxsorb III/R32 and Maxsorb III/R134a pairs compared to the other pairs. In that sense, ACF-A20/R32, Maxsorb

III/R134a and Maxsorb III/R32 pairs can be considered as a more suitable choice over the ACF-A20/R134a and Maxsorb III/n-butane pairs in designing a practical adsorption cooling system when only considering the isosteric heat of adsorption. A lower isosteric heat of adsorption would require less energy to maintain the bed temperature for adsorption to happen. However, Maxsorb III/n butane and ACF-A20/R32 pairs can act as suitable choice for heating applications because the heat generated from the isosteric heat of adsorption can be used for heating the space as well.

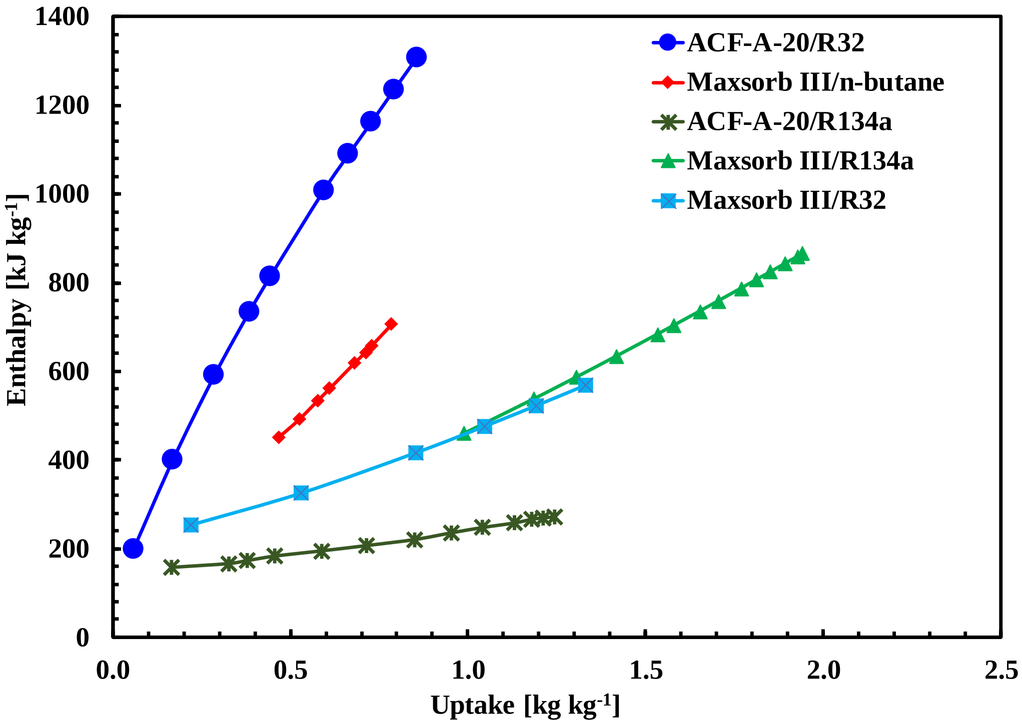

Figure 1.4 Comparison of enthalpy map.

Enthalpy and entropy maps with the uptake of the discussed pairs are obtained at 298.15 K using equations (31) and (46) which are depicted in Figure 1.4 and Figure 1.5, respectively. All five adsorption pairs show that the enthalpy and entropy of a single component adsorbate-adsorbent system always increase with the increasing uptake. However, ACF-A20/R32 pair shows the highest rate of change of enthalpy with respect to the uptake, whereas enthalpy of ACF-A20/R134a pair remains relatively steady. So considering the enthalpy, it can be concluded that ACF-A20/R32 pair is the most preferred pair in designing a practical adsorption chiller.

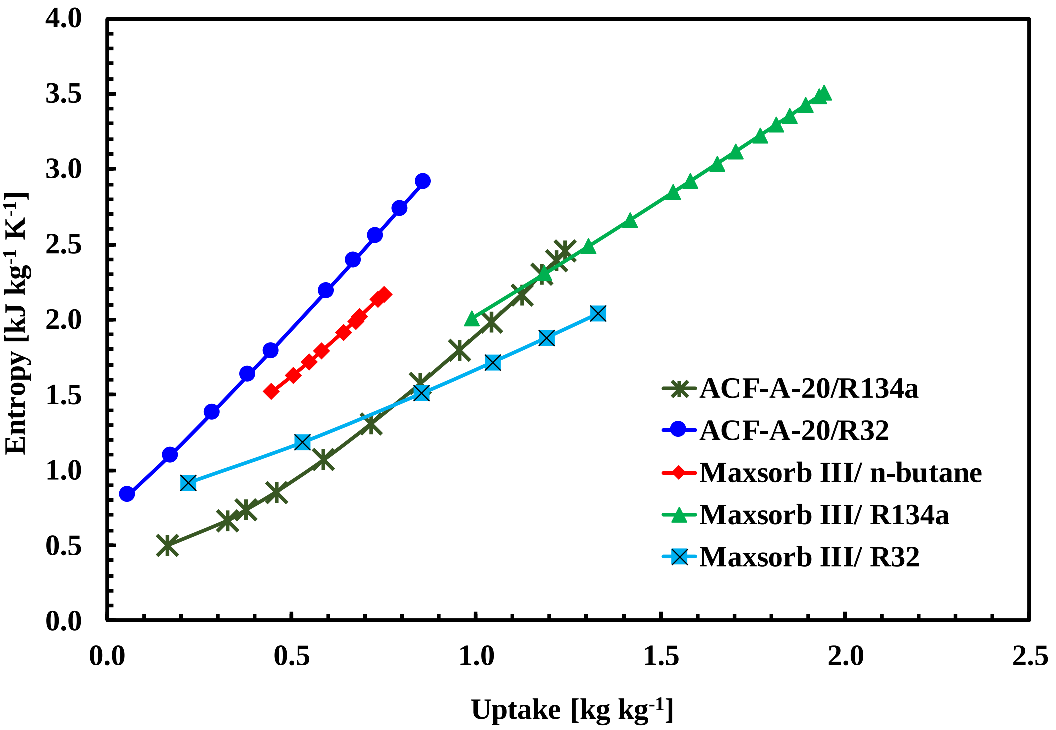

Figure 1.5 Comparison of entropy map.

However, figure 1.5 illustrates that ACF-A-20/R32 and Maxsorb III/n-butane pairs have a higher increase in entropy with increasing uptake. Maxsorb III/ R134a pair shows comparatively moderate increase of entropy with uptake considering the previous two pairs. Contrarily, ACF-A-20/R134a and Maxsorb III/ R32 pairs exhibit a relatively steady entropy increase with uptake. However, in the lower uptake regions from, 0.1 kg kg^{-1} to 0.8 kg kg^{-1} ACF-A-20/R134a pair manifests the lowest values of entropy whereas, in slightly higher uptake range from 0.8 kg kg^{-1} to 1.4 kg kg^{-1} Maxsorb III/ R32 pair exhibits the lowest entropy among all the pairs. This result suggests that the practical adsorption chiller should be designed considering the ACF-A20/R134a or Maxsorb III/ R32 pair respectively depending on the cooling load required.

The T-s maps for the adsorption characteristics of Maxsorb III/n-butane, ACF-A20/R134a, ACF-A20/R32, Maxsorb III/R134a and Maxsorb III/R32 systems are shown in Figures 1.6(a), (b), (c), (d) and (e) respectively where ABCDA represents the adsorption cooling cycle in terms of entropy as a function of T and q ($q=m_a/M$) (neglecting the effect of pressure). All the diagrams are plotted considering an operating condition of 5 °C cooling.

During regeneration phase (lines a-b-c), the pressure in the adsorber bed rises from P_{evap} to P_{cond} by heating the adsorber bed. The refrigerant desorbs and gets condensed in the condenser. The amount of adsorbed uptake falls from q_{ads} to q_{des}, and the entropy rises from s_{ads} to s_{des}. Contrarily, during the adsorption phase, following the path DAB, the adsorber bed is cooled, and the pressure falls from P_{cond} to P_{evap}. Then, the refrigerant vapour is adsorbed on the adsorbent and the amount adsorbed again increases up to q_{ads} from q_{des}. It is also found from the present analysis that the entropy flow, $\Delta s\left(=s_{ads}-s_{des}\right)$ in the Maxsorb III/n-butane, ACF-A20/R32, Maxsorb III/R32 systems, are higher than that of the other two systems- ACF-A20/R134a and Maxsorb III/R134a. This suggests that relatively higher energy is required to drive the adsorption cooling systems with ACF-A20/R32, Maxsorb III/R32 and Maxsorb III/ n-butane Adsorbent/ refrigerant pairs when compared with ACF-A20/R134a and Maxsorb III/R134a adsorbent/adsorbate pair associated systems.

If the cooling load is changed to 10 °C and 15 °C the difference between uptake and offtake become larger and the entropy flow reduces. Moreover, the area of operation also increases. This is shown in Figure. 1.6(f) and (g) for 10 °C and 15 °C respectively for ACF-A20/R134a pair with green shades. The rest of the pairs also show similar improvements. The key parameters for the T-s diagrams for all the cooling conditions are summarized in table 1.4.

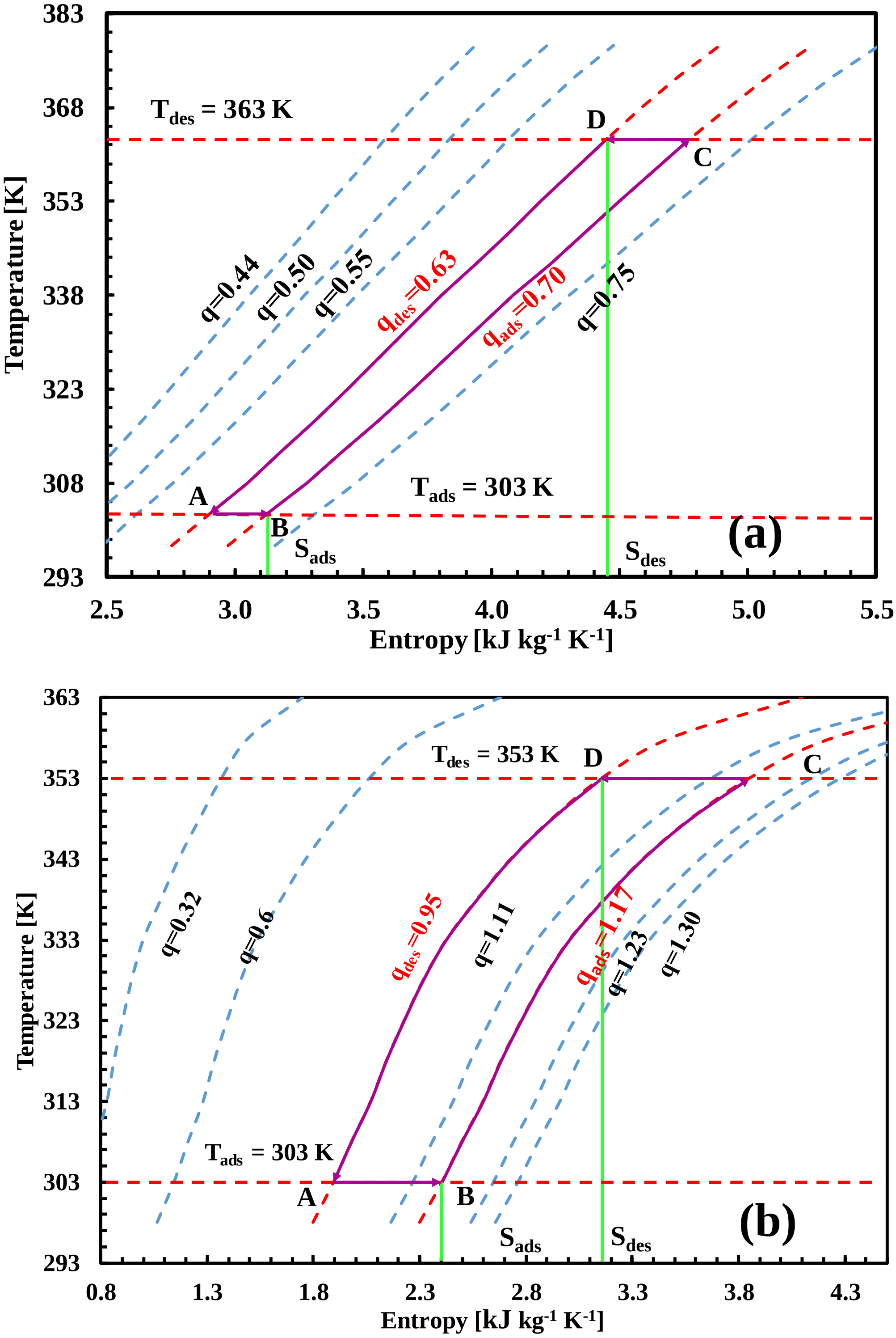
383
368
353
338
323
308
293
Temperature [K]
T_{des} = 363 K
D
C
q=0.44
q=0.50
q=0.55
q_{des}=0.63
q_{ads}=0.70
q=0.75
T_{ads} = 303 K
A
B
S_{ads}
S_{des}
(a)
2.5
3.0
3.5
4.0
4.5
5.0
5.5
Entropy [kJ kg^{-1} K^{-1}]
363
353
343
333
323
313
303
293
Temperature [K]
T_{des} = 353 K
D
C
q=0.32
q=0.6
q_{des}=0.95
q=1.11
q_{ads}=1.17
q=1.23
q=1.30
T_{ads} = 303 K
A
B
S_{ads}
S_{des}
(b)
0.8
1.3
1.8
2.3
2.8
3.3
3.8
4.3
Entropy [kJ kg^{-1} K^{-1}]

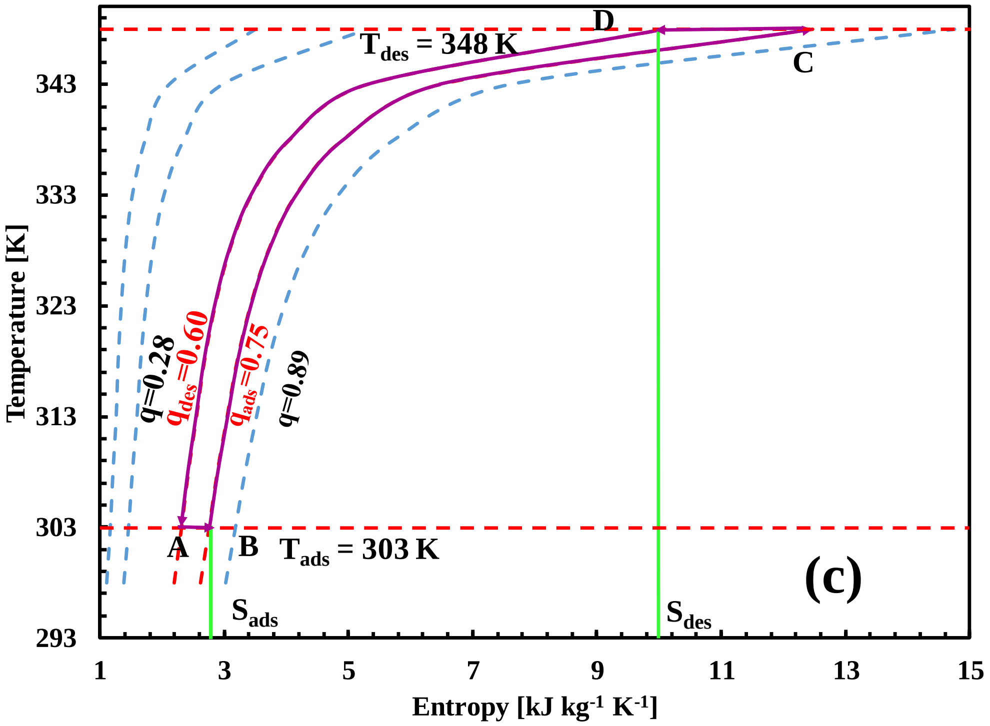
Temperature [K]
343
333
323
313
303
293
1
3
5
7
9
11
13
15
Entropy [kJ kg-1 K-1]
D
Tdes = 348 K
C
q=0.28
qdes=0.60
qads=0.75
q=0.89
A
B
Tads = 303 K
Sads
Sdes
(c)

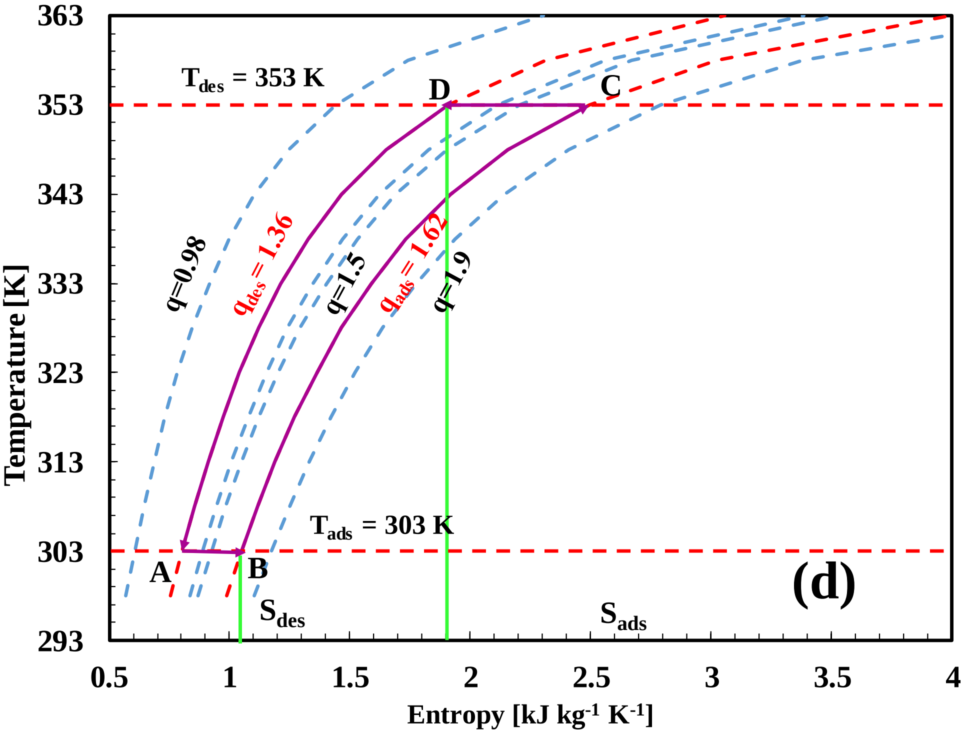
363
353
343
333
323
313
303
293
Temperature [K]
0.5
1
1.5
2
2.5
3
3.5
4
Entropy [kJ kg-1 K-1]
Tdes = 353 K
D
C
q=0.98
qdes = 1.36
q=1.5
qads = 1.62
q=1.9
Tads = 303 K
A
B
Sdes
Sads
(d)

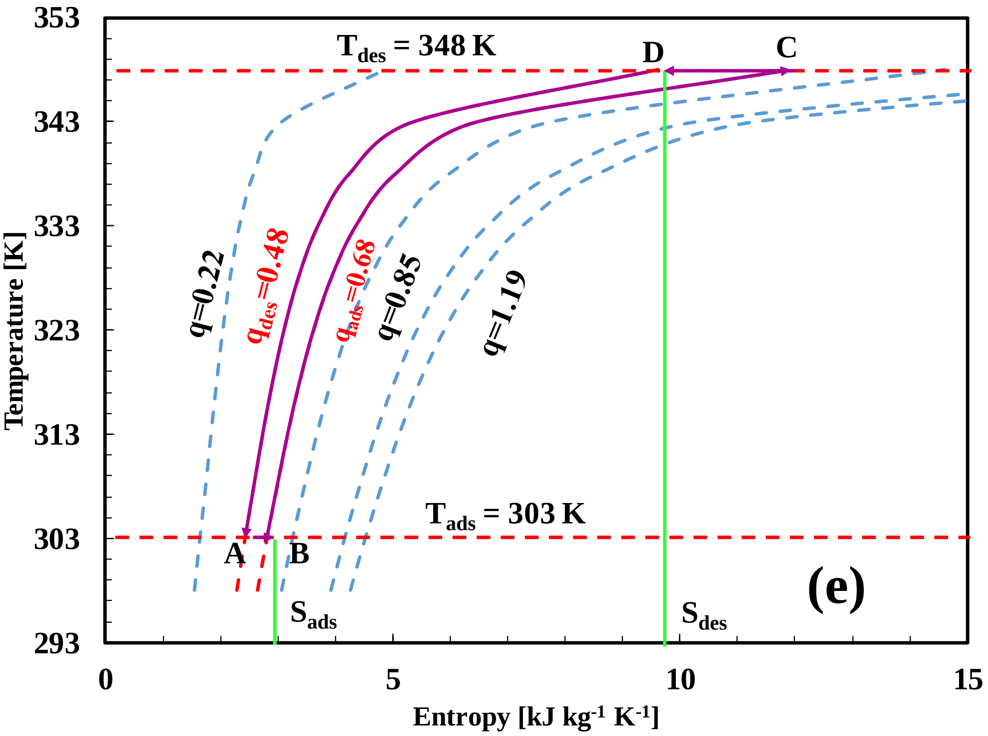
Temperature [K]
353
343
333
323
313
303
293
0
5
10
15
Entropy [kJ kg-1 K-1]
Tdes = 348 K
D
C
q=0.22
qdes=0.48
qads=0.68
q=0.85
q=1.19
Tads = 303 K
A
B
Sads
Sdes
(e)

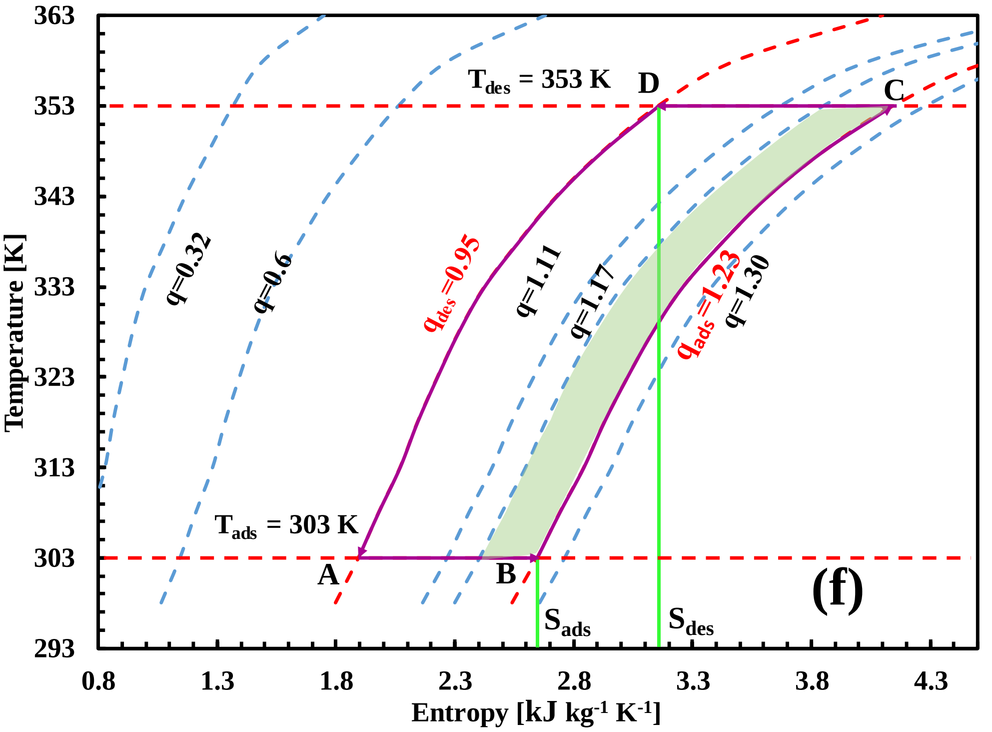
Temperature [K]
363
353
343
333
323
313
303
293
0.8
1.3
1.8
2.3
2.8
3.3
3.8
4.3
Entropy [kJ kg-1 K-1]
Tdes = 353 K
D
C
q=0.32
q=0.6
qdes=0.95
q=1.11
q=1.17
qads=1.23
q=1.30
Tads = 303 K
A
B
Sads
Sdes
(f)

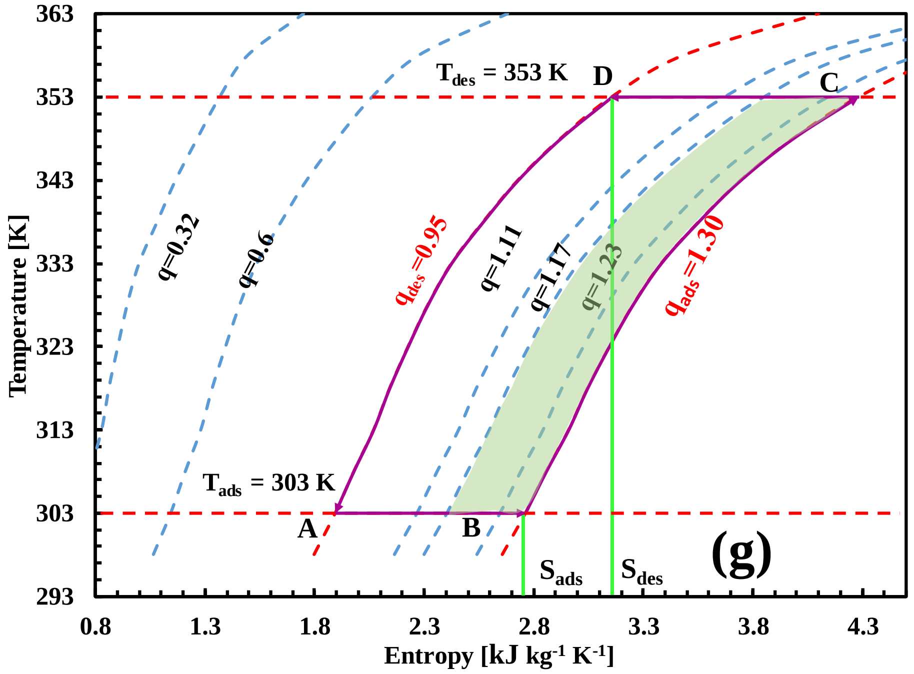

Figure 1.6. (a)-(e) T-s diagram considering 5 °C cooling for Maxsorb III/n-butane, ACF-A-20/R134a, ACF-A-20/R32, Maxsorb III/R134a, Maxsorb III/R32 paired system, respectively; (f) and (g) T-s mapping for ACF-A-20/R134a paired system for 10 °C cooling and 15 °C cooling, respectively.

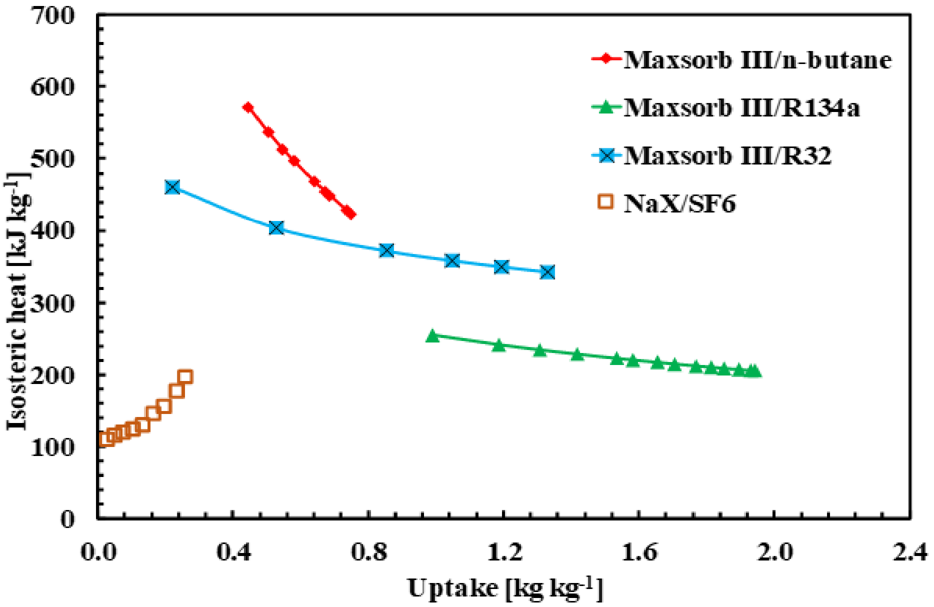

Figure 7. Variations in isosteric heat for different refrigerants pairing with a conventional adsorbent (MAXSORB III).

Table 1.4. T-s maps defining parameters.

	Adsorption pairs	**P_{cond} [kPa]**	**P_{eva} [kPa]**	**$q_{ads} = f(P_{evap}, T_{ads})$ [kg kg^{-1}]**	**$q_{des} = f(P_{cond}, T_{des})$ [kg kg^{-1}]**	**Δq [kg kg^{-1}]**	**Entropy flow [kJ kg^{-1} K^{-1}]**
T_{eva} = 5 °C	Maxsorb III/ n-butane	283.41	124.25	0.70	0.63	0.07	1.35
	Maxsorb III/ R134a	770.2	349.66	1.62	1.36	0.26	0.8
	Maxsorb III/ R32	1927.5	951.45	0.68	0.48	0.20	6.8
	ACF-A20/ R134a	770.2	349.66	1.17	0.95	0.22	0.75
	ACF-A20/ R32	1927.5	951.45	0.75	0.60	0.15	7.4
T_{eva} = 10 °C	Maxsorb III/ n-butane	283.41	148.45	0.73	0.63	0.1	1.2
	Maxsorb III/ R134a	770.2	414.61	1.70	1.36	0.34	0.75
	Maxsorb III/ R32	1927.5	1106.9	0.75	0.48	0.27	6.5
	ACF-A20/ R134a	770.2	148.45	1.23	0.95	0.28	0.5
	ACF-A20/ R32	1927.5	1106.9	0.80	0.60	0.20	7.0
T_{eva} = 15 °C	Maxsorb III/ n-butane	283.41	176.15	0.75	0.63	0.12	1.13
	Maxsorb III/ R134a	770.2	488.37	1.77	1.36	0.41	0.70
	Maxsorb III/ R32	1927.5	1280.8	0.82	0.48	0.34	6.4
	ACF-A20/ R134a	770.2	488.37	1.30	0.95	0.35	0.4
	ACF-A20/ R32	1927.5	1280.8	0.86	0.60	0.26	6.9

The isosteric heat of adsorption was compared for three different adsorbates: n-butane, R32 and R134a pairing with a common adsorbent Maxsorb III in Figure 1.7 along with isosteric heat of adsorption of SF_6.in NaX [25,50]. Contributions of different adsorbate molecules causing variation in thermodynamic property fields were investigated here. One interesting observation was; the more fluorine atoms present in the adsorbate molecules results in having a steadier isosteric heat of adsorption. In case of an R32 molecule there are 2 fluorine atoms resulting in a steady isosteric heat profile. R134a molecule contains 4 fluorine atoms resulting in a steadier isosteric heat profile whereas, SF_6 molecule having 6 fluorine atoms has its isosteric heat increasing with the surface coverage. One possible reason for this could be the highly electronegative fluorine atoms neutralizing the van der Walls forces created by the surface atoms of the adsorbents. Another reason behind this could be the states of the adsorbates. Both R32 and R134a refrigerants remain in their superheated gaseous phase. As a result, the gas-solid interaction between the refrigerant /carbonaceous adsorbent pair becomes weaker than that of the gas-gas interaction (among refrigerant molecules). This dominant gas-gas interaction causes increase in the isosteric heat of adsorption. Initially, the effect of this increase in isosteric heat is negligible. Whereas, at higher uptake, this increase in isosteric heat of adsorption affects the usual decreasing trend of isosteric heat of adsorption profile by making it more steady. This completely agrees with the adsorption data of SF_6 in NaX in published literature [25,50].

1.4 CONCLUSION

The thermodynamic characteristics such as entropy and enthalpy of single component adsorbate-adsorbent systems were investigated based on some well-established mathematical models. It was observed that the entropy and enthalpy of the adsorbed phase increased with the uptake whereas the isosteric heat of adsorption decreased. Furthermore, this study showed that the number of fluorine molecules has an indistinguishable effect on the isosteric heat of adsorption. Change of isosteric heat profile depends on the number of fluorine atoms present in the refrigerant molecule. With no fluorine atom the isosteric heat of adsorption decreases sharply with uptake (Maxsorb III/n-butane). With two fluorine atoms (for R32) it becomes a bit steadier. For R134a where there are four fluorine atoms it is more steady. However, for SF_6 adsorption in NaX the six fluorine atoms cause the isosteric heat of adsorption increase with uptake instead of decreasing. This happens because the high electronegative fluorine atoms are responsible for making the gas-gas interaction more dominant than the gas-solid interaction. T-s mapping for all the pairs for different cooling conditions lead to some interesting results. When the evaporation temperature is changed from 5 °C to 10 °C the difference between uptake and offtake become larger resulting in an increment of the operating area. The entropy flow also reduces ensuring less power to drive the system. In addition, if the evaporation temperature is changed from 10 °C to 15 °C the improvements are higher. Apart from the kinetics and adsorption isotherms, the thermodynamic property fields could also play a vital role in selecting a proper adsorbent/refrigerant pair for a specific application. This, in turn, opens a door for optimization studies regarding adsorption system. Moreover, this information can be used to analyze the energy balance and adsorption equilibrium which are essential for the rigorous design of an adsorption cooling system.

ACKNOWLEDGEMENT

The initial author acknowledges the Kyushu University Program for Leading Graduate School: Green Asia Education Center for financial support.

CHAPTER 2

Synthesis and Characterization of Aluminum Fumarate Metal Organic Framework

CHAPTER 2

Synthesis and Characterization of Aluminum Fumarate Metal Organic Framework

Microporous metal-organic frameworks (MOFs) having higher difference between adsorption and desorption uptake per cycle are considered as one of the most potential adsorbents for future designing of adsorption heat pumps. In this study, aluminum fumarate was synthesized using a green reaction (water was used as solvent instead of DMF) involving hydrothermal process. In case of water adsorption on this green synthesized aluminum fumarate, s- shaped isotherm was obtained. This s-shaped isotherm ensured the difference between uptake and offtake to be large within a narrow pressure range. The newly synthesized aluminum fumarate shows higher water uptake and enhanced porous properties than the commercially available now.

2.1 INTRODUCTION

MOFs are highly crystalline powdered like materials having high surface area and pore volume. These materials are moderately stable and can be synthesized in their very pure form [51–53]. As a result, they become great potential materials for various applications involving microporous materials such as catalysis [54,55], gas separations and storage [56–59], sensors [60] and heat pumps [61,62]. As the MOFs are known to possess high surface area and pore volume they fulfil one of the basic conditions to be an adsorbent for adsorption chiller. Water adsorption has been done on number of MOFs including ISE-1, HKUST-1, MIL-100(Fe), MIL-53(Fe), Basolite 100A and Basolite F300. And they showed better performance when compared with silica gel and zeolite [63–65]. Thus

MOFs are becoming more and more popular for water assisted AHT applications. The pore diameter and hydrophilicity plays an important role in water adsorption in an adsorbent. The adsorbents with pore diameter below the critical (20.76 Å) for water, [66] would trigger water adsorption in the pores without condensation. Moreover, hydrophilicity in the pore must be adequate to allow water nucleation and pore filling below the relative pressure (P/Ps) of 0.3 for AHT applications [61,67].

Recently, Aluminum Fumarate (Al-Fum), an aluminum based MOF was synthesized and patented by Kiener et al. However, the water adsorption on Al-Fum is high at relatively higher pressures.

Alvarez et al. [68] had compared the adsorption characteristics of Al-Fum with MIL-53(Al) by experimenting its selectivity with ethanol. Jeremias et al. [69] had synthesized Al-Fum adsorbents with additional coating for higher stability and thermal conductivity. Elsayed et al. [70] compared the water adsorption capability of Al-Fum with CPO-27(Ni) at 25 °C under static and dynamic conditions. Both materials were found suitable for adsorption heat pump and desalination applications from simulation viewpoints.

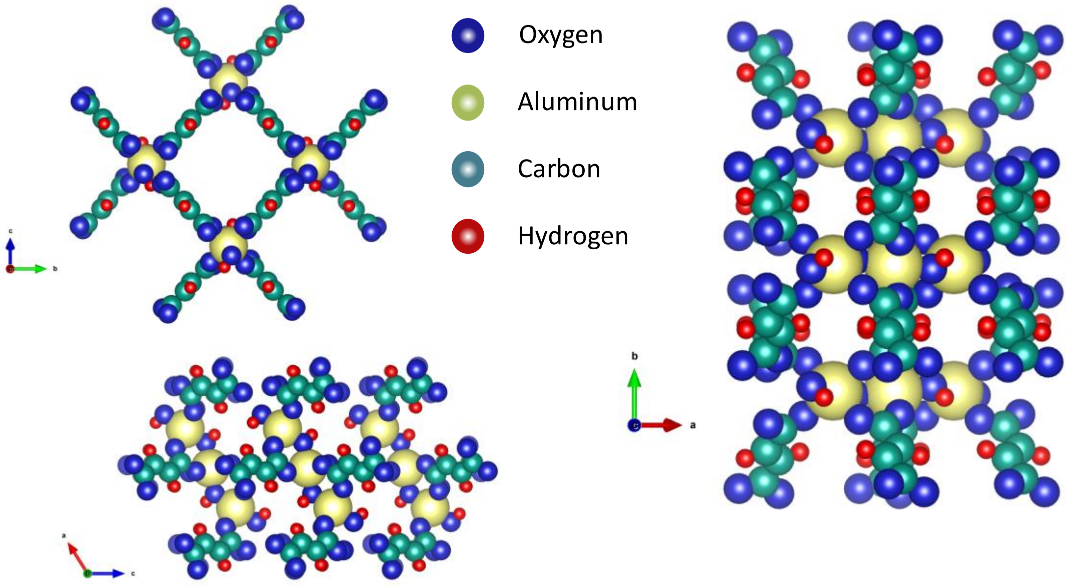

Figure 2.1 3D view of Aluminum Fumarate

In this study, we have modified the synthesis procedure for Aluminum fumarate prescribed in the patent. The porous properties are characterized by SEM, XRD and N2 adsorption isotherm analysis. To observe the amount of water uptake on Al-Fum MOF, water adsorption experiment is conducted by a thermogravimetric method for 30 °C, 50 °C and 70 °C temperatures and pressures up to the saturated region. All the experiments were also done for commercially available aluminum fumarate for comparing data with our synthesized one.

2.2 EXPERIMENTAL SETUP

2.2.1 Materials

Aluminum sulfate octadecahydrate ($Al_2(SO4)_3.18H_2O$, 57.5%, Waco Pure Chemical Industries), fumaric acid (COOH−CH═CH−COOH, 98%, Waco Pure Chemical Industries) and sodium hydroxide (NaOH, Sigma Aldrich co) were used for synthesis of Aluminum Fumarate. Deionized water was used as a solvent. All the reagents were of analytical grade and were used as it was supplied without further purification.

2.2.2. Synthesis

For synthesizing Aluminum fumarate 7 gm of $Al_2(SO4)_3.18H_2O$ (0.0105 mol) was dissolved in 30 ml of deionized water at room temperature in a glass beaker and heated to 60°C using an electric heater. Next, 2.63 gm of fumaric acid (0.0227 mol) and 2.73 gm of NaOH (0.0683 mol) were mixed in 39 ml of water and dissolved by stirring. NaOH helps in deprotonation of fumaric acid. The solution was heated to 60°C and was added to the solution of fumaric acid dropwise with stirring at 250 RPM for 16 minutes. White milk like the suspension was observed. The product was separated from the reaction mixture by centrifugation at 5000 RPM for 20 minutes and washed with water for 3 times to remove any unreacted reagents. The product was collected in a glass petri dish and dried in a vacuum oven at 100°C for 8 hours. The product was powdered using a mortar and pestle. Finally, the powder was activated at 150°C in a vacuum oven for 8 hours.

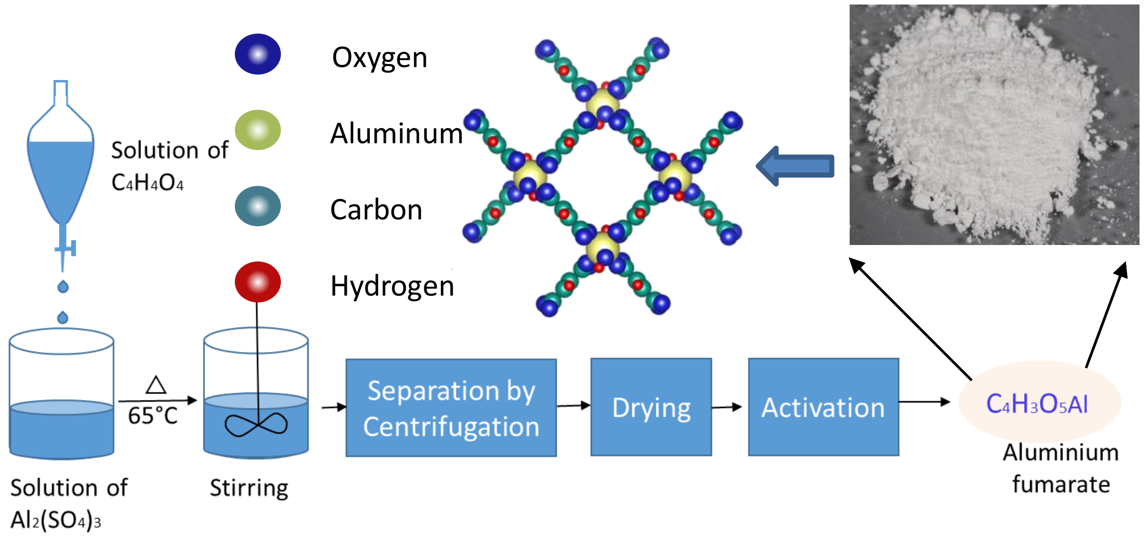

Figure 2.2 Hydrothermal synthesis of Aluminum fumarate MOF.

2.2.3 Characterization

2.2.3.1 XRD and FESEM

The microstructure and morphologies of the samples were determined by JEOL JSM-7900F FESEM (Field Emission Scanning Electron Microscopy) operated at 3 kV. Powder X-ray diffraction (PXRD) analysis were performed on a Rigaku SmartLab 9kW AMK using monochromatic CuK_α radiation with a step size of 0.02˚, the operated wave length was 1.54 Å at 40 kV and 30mA.

The pore size, pore volume and specific surface area of samples were measured by N_2 adsorption/desorption isotherms at 77K. The samples were degassed at 120˚C for 3h prior to N_2 adsorption measurement. The N_2 adsorption/desorption isotherm of synthesized composites has been investigated using volumetric method employing 3Flex™ Surface Characterization Analyzer as shown in Fig. 2.3. The pore size distribution is determined using NLDFT (Non Localized Density Functional Theory) from the N_2 adsorption isotherms. The total pore volume is obtained by N_2 adsorption data under saturation conditions. If the isotherm is nearly horizontal throughout the range of P/P_s as it approaches to saturation, macro pores are not found in the adsorbent structure. Hence, the pore volume is defined properly. With the existence of macro pores, the isotherm will have a sharp increase as P/P_s approaches to 1. The limiting uptake of the isotherm is used to identify as the total pore volume of adsorbent.

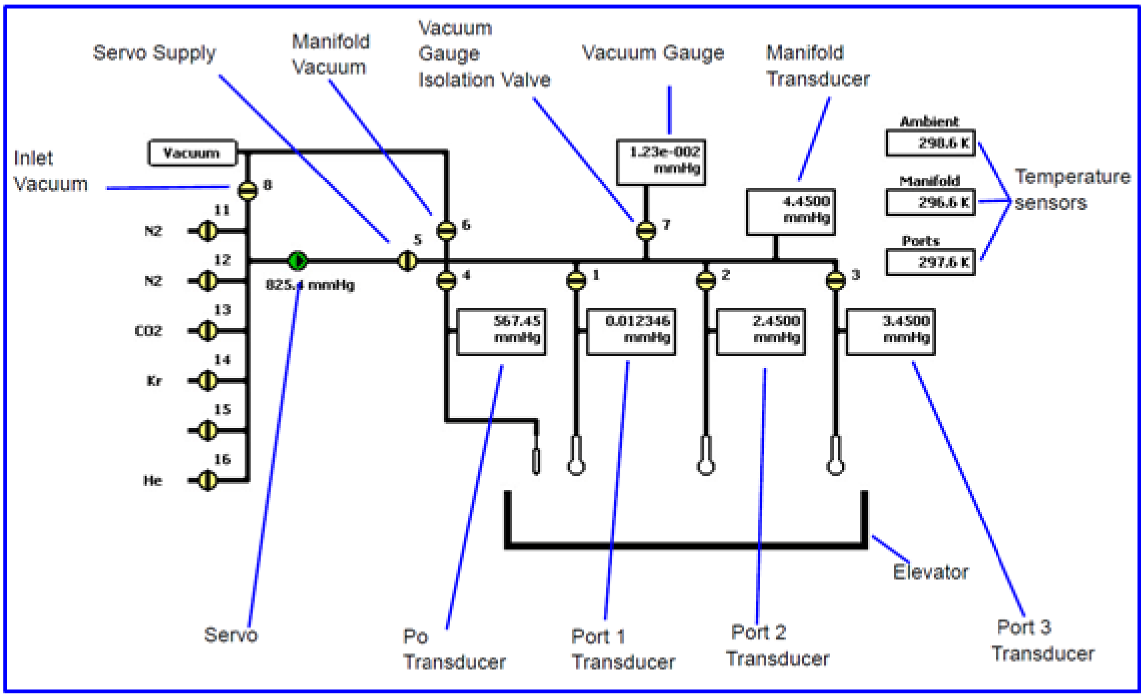

Figure.2.3 Schematic diagram of 3Flex™ Surface Characterization Analyzer.

2.2.3.2 Water adsorption

The amount of water vapor on Al-Fum MOF at different temperatures and pressures are measured by a thermogravimetric analyzer (TGA) due to the high accuracy and ease of control of pressure and temperature during experimentation. We have used the magnetic suspension adsorption measurement unit (Rubotherm of type MSB-VG-S2) supplied by BEL Japan, Inc. Figure. 2.4. shows the schematic diagram of the magnetic suspension adsorption measurement unit. Experimental procedure [19] can be explained as follows;

(1) We have measured water adsorption isotherms for both commercially available aluminum fumarate and our synthesized aluminum fumarate.

(2) First, the commercial sample of 65 mg was put into the sample basket and placed into the measuring chamber of the magnetic suspension balance unit.

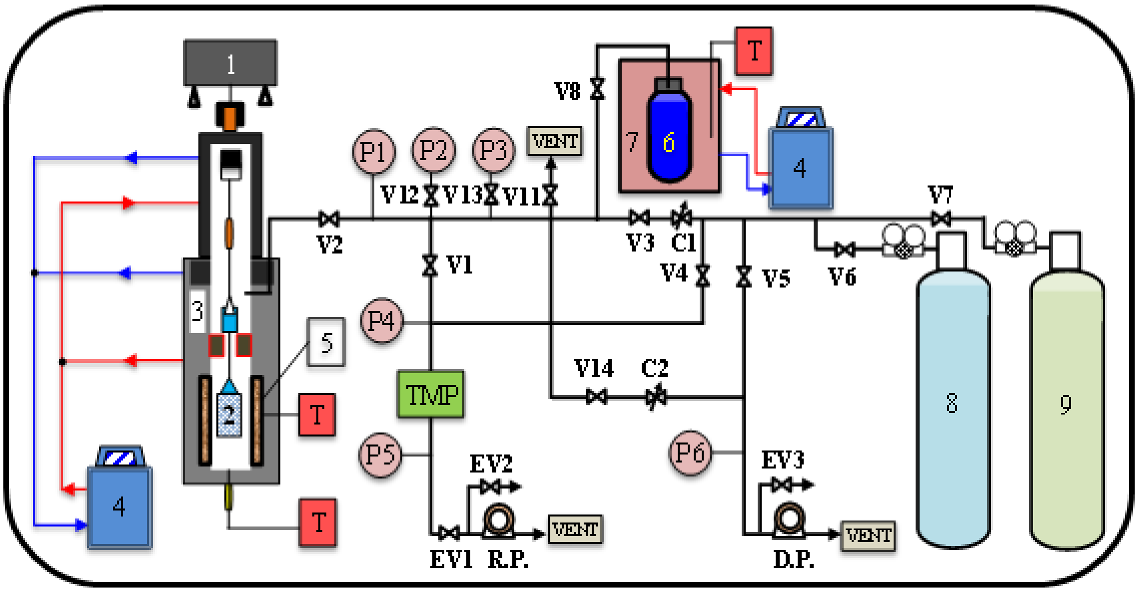

1. Magnetic suspension balance; 2. Sample cell; 3. Circulation oil jacket; 4. Oil bath and circulator; 5. Sheathed heater; 6. Refrigerant container; 7. Isothermal oil bath; 8. Helium; 9. Nitrogen; TMP: Turbo-molecular pump; R.P.: Rotary pump; D.P.: Diaphragm pump; T: Thermocouple; P1-P6: Pressure gauges; C1-C2: Controlled valves; V1-V13: Valves.

Figure 2.4 Schematic diagram of experimental apparatus.

(3) The sample was regenerated at 100 °C under vacuum conditions for about 4hrs. then the sample was cooled down to the set adsorption temperature where the measuring chamber is disconnected from the vacuum pump units.

(4) The measuring chamber was connected to the evaporator chamber. Evaporator temperature was controlled using an oil bath. Pressure of measuring chamber increased rapidly until it reached the evaporator pressure corresponding to the set evaporator temperature. Adsorption process was then carried out where adsorbent mass was recorded continuously until reaches to the adsorption equilibrium conditions.

(5) Evaporator is then disconnected from the adsorption chamber where its temperature increases to a certain value to create a new evaporation pressure for the next measuring step.

(6) Steps (3) – (5) were repeated for other sets of adsorption temperatures.

(7) Same procedure was also carried out for our synthesized aluminum fumarate sample.

2.3 RESULTS AND DISCUSSION

2.3.1. XRD and FESEM characterization:

Figures 2.5(a) and 2.5(b) show the SEM (scanning electron microscopy) diagram for commercial aluminum fumarate and our synthesized one respectively. The size of the sample is about 1 µm with quadrahedral shape. The shape synchronizes with the molecular structure of aluminum fumarate [68]. Hence, this proves that aluminum fumarate is synthesized correctly.

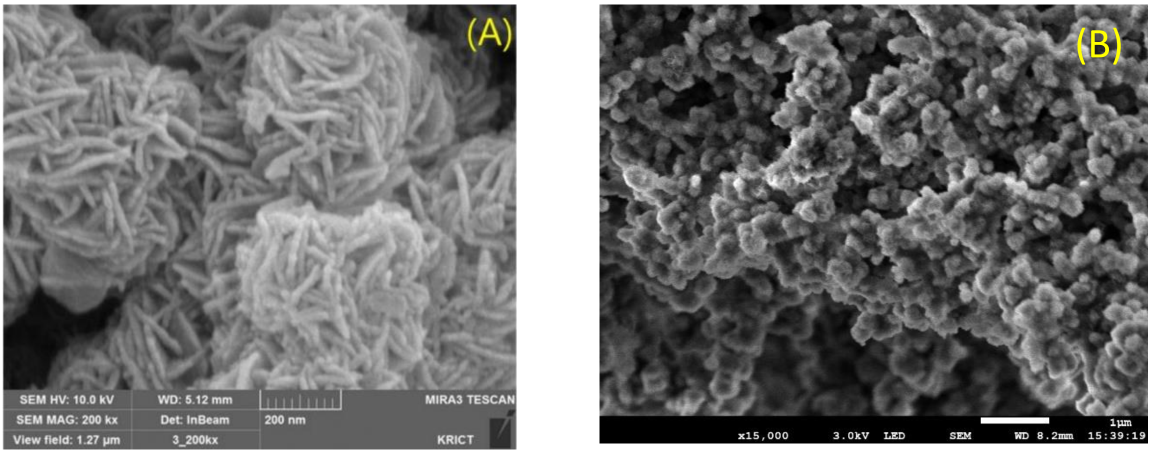

Figure 2.5 SEM images of (a) Commercial aluminum fumarate [68] *(b) our synthesized aluminum fumarate*

Figure 2.6 shows the PXRD (Powder X-ray Diffraction) graphs of the Al-Fum. The first peak can be seen at 10 ° with small peaks shown at higher angles. The peaks correlate the intensity of Al^{3+} in the adsorbent structure. It also shows that the purification of the material was properly done. Thus, the material structure is stable as no additional peaks are detected.

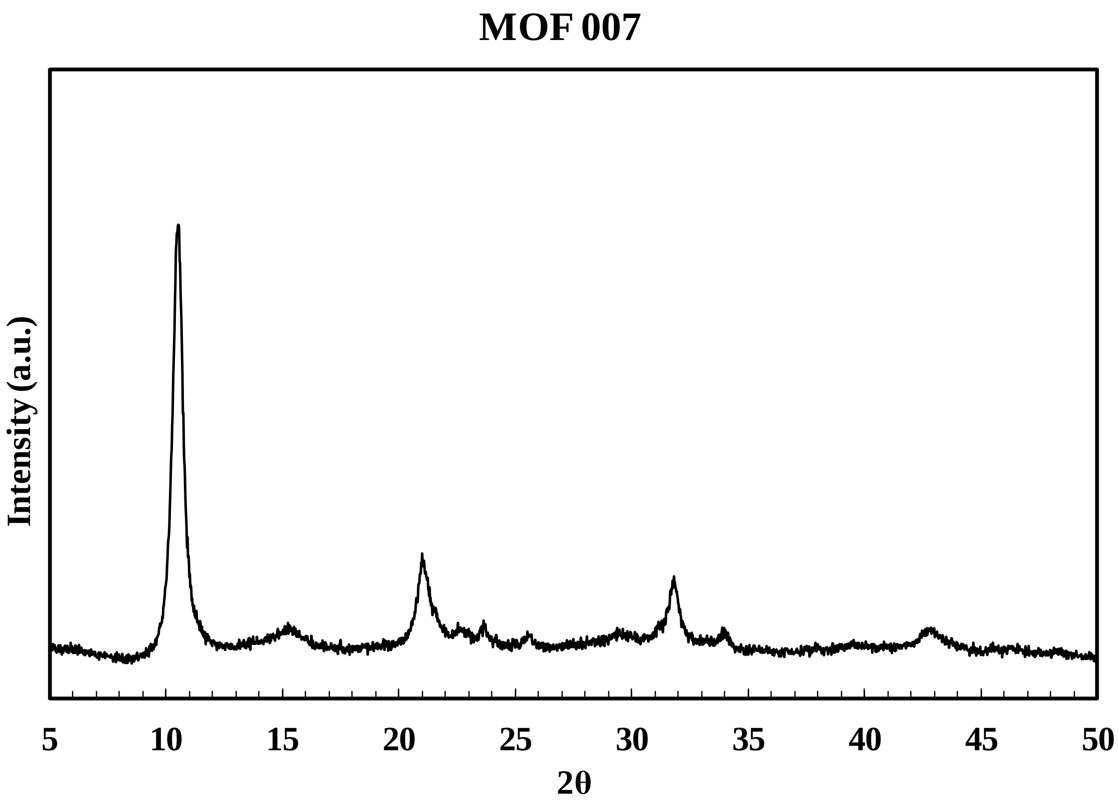

Figure 2.6 XRD image of synthesized aluminium fumarate

2.3.2. N_2 adsorption

Figure 2.7 and 2.8 show the N_2 adsorption-desorption isotherm on commercial and synthesized aluminum fumarate adsorbent. From the experimental data, it is found that on each case the volumetric N_2 uptakes for both the samples are within 12 mmol/g of adsorbent before approaching to saturated pressure. As approaching towards the saturated pressure, the volumetric uptake increases up to approximately 17 and 16 mmol/g of sorbent respectively. This suggests that the material has large variations of micropores and macropores within their structures. One more interesting fact can be observed from the two above mentioned figures is that in commercial sample there is some hysteresis in N_2 adsorption where as in case of synthesized sample the amount of hysteresis is reduced. The pore width, pore volume and surface area are calculated employing BET analysis and N_2 adsorption data. These are shown in table 2.1. In Figures 2.9 (a) and (b) the pore size distributions of the two samples and they agree with the crystallographic data in figure 2.9

(c).

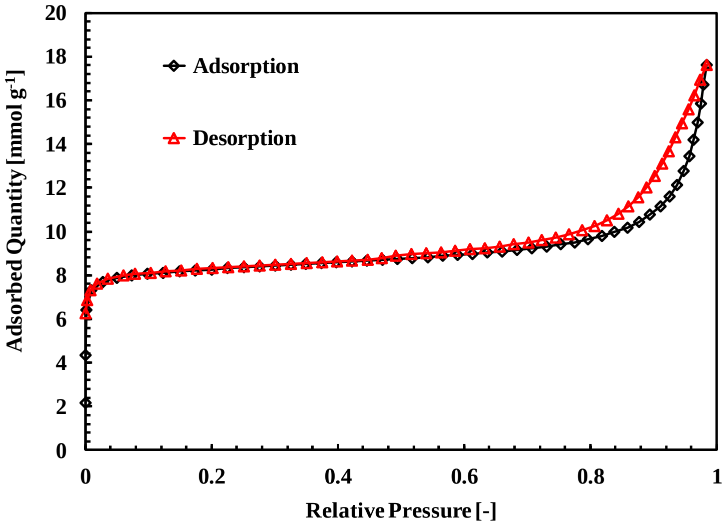

Figure 2.7 N_2 adsorption-desorption on commercial aluminum fumarate at 77K

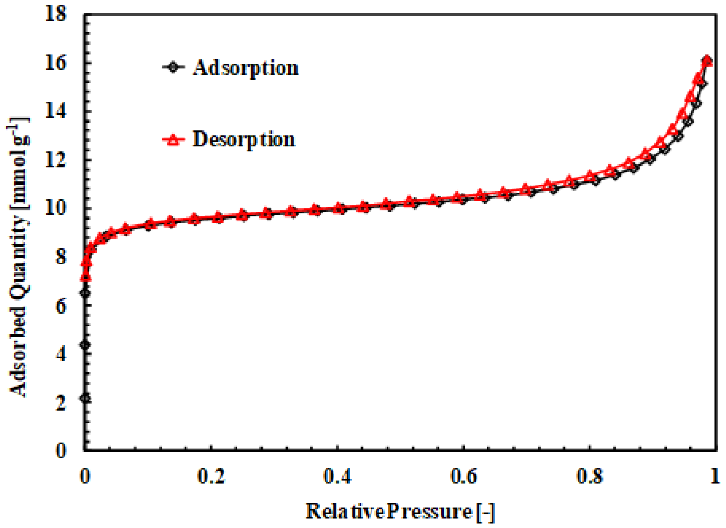

Figure 2.8 N_2 adsorption-desorption on our synthesized aluminum fumarate at 77K

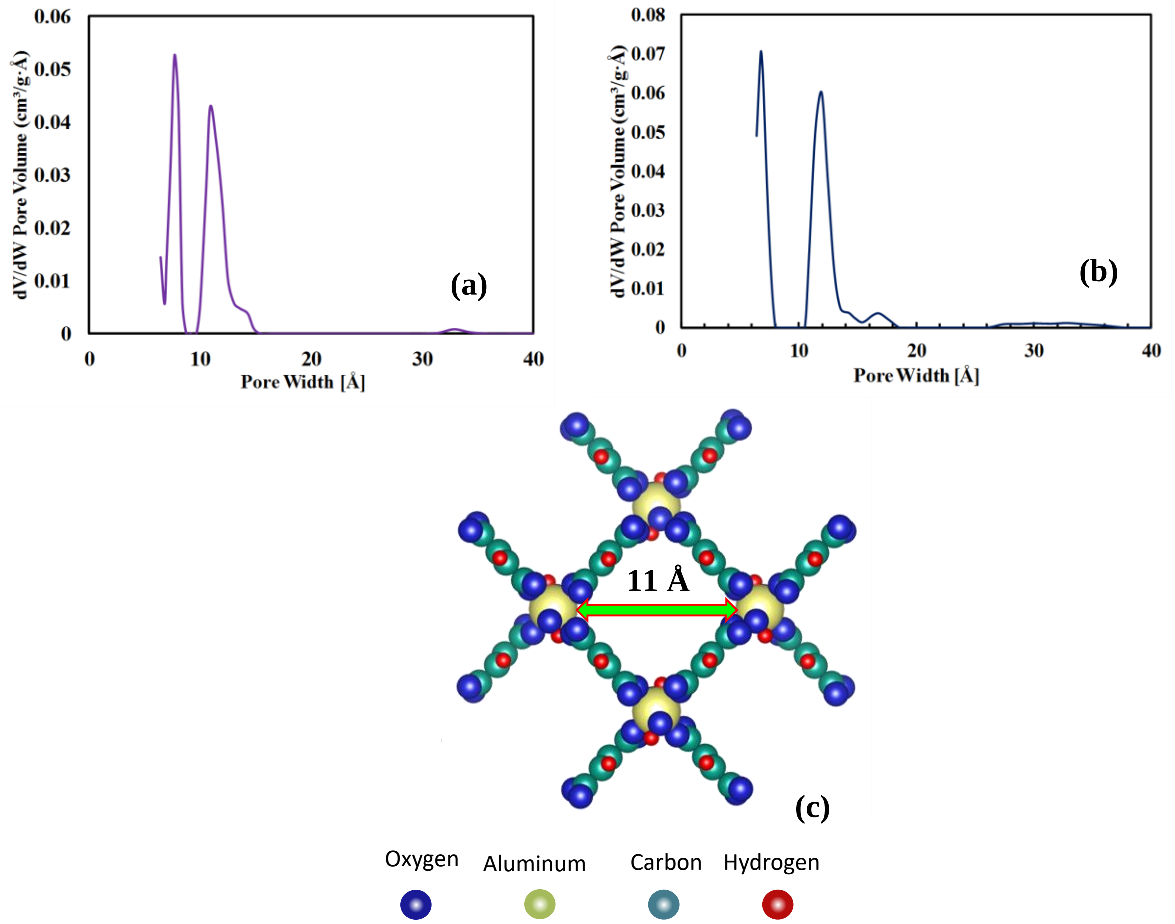

Figure 2.9 Pore size distribution of (a) commercial aluminum fumarate (b) our synthesized aluminum fumarate (c) pore size measured from crystallographic data of aluminum fumarate.

Table 2.1 Porous properties of the commercial and synthesized aluminum fumarates.

Sample	**BET surface area** **[m^2g^{-1}]**	**Average pore width** **[Å]**	**Pore volume** **[cm^3g^{-1}]**
Commercial Al-Fum	600	11	0.58
Synthesized Al-Fum	674	11	0.53

2.3.3 Water adsorption isotherm

Water adsorption isotherms were measured for both the commercial and our synthesized aluminum fumarate samples. The results are shown in Figure 2.10. In both cases, we obtained S-shaped isotherms that are the desired one for adsorption chiller application.

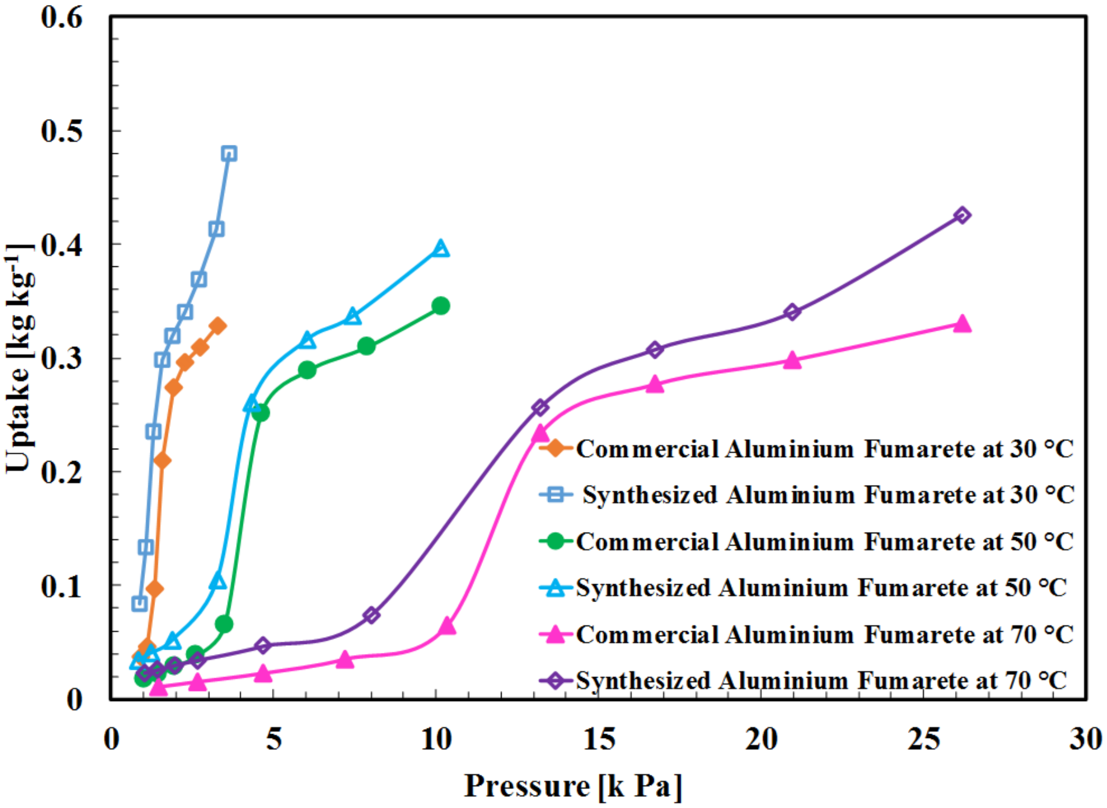

Figure 2.10 Water adsorption isotherms comparison between commercial and our synthesized aluminum fumarate.

However, in every cases the uptake of our synthesized aluminum fumarate was higher than that of the commercially available sample. Moreover, for the synthesized sample the isotherms also shift towards lower pressure region making it more suitable for practical application. This is because the lower the pressure the less chances of leakage. The reason behind this could the related to the increase of surface area. This could have happened because of the green synthesis approach.

2.4. CONCLUSION

In this study, we have shown that we have successfully synthesized aluminum fumarate using a green synthesis approach. The XRD and SEM images matched well with the published literature confirming its reliability. The pore size distribution matched well with the commercial sample. In our synthesis process, we managed to increase the surface area about 10 % than the commercial sample. Because of that, the water uptake also increased. However, this study shows that the isotherms can be shifted towards the lower pressure region. This could lead to a new scope of research, as MOFs properties are highly tunable. The various ways of modification can help in shaping the isotherms as well as shifting them to our desired ones.

CHAPTER 3

Surface structure determination of clean Pd (111) using low energy electron diffraction (LEED)

CHAPTER 3

Surface structure determination of clean Pd (111) using low energy electron diffraction (LEED)

The surface relaxation of clean Pd(111) surface is determined using quantitative low energy electron diffraction (LEED) analysis. The cleanliness of the surface is confirmed using Auger electron spectroscopy (AES). We collected experimental data for 5 symmetrically independent beams, covering a cumulative energy range of 841 eV. With a minimum Pendry reliability factor $R_p \simeq 0.14$, we found that the first six atomic layers showed sequence of expansion (+) and contraction (-) of (+; +; +; -; +; +), as compared to the bulk-truncated interlayer spacing of 2.2452 Å. The determination of this relaxation sequence is important for understanding the structural growth of 2D materials such as plumbene on Pd(111).

3.1 INTRODUCTION

The surface of a crystalline surface in vacuum is generally defined as the few, approximately three or four, outermost atomic layers of the solid. The surface properties vary significantly from the bulk due to the difference in coordination number. The surface may be entirely clean or it may have forcing atoms deposited on it or incorporated in it. In macroscopic materials, the bulk electronic structure determines most materials properties, with negligible influence of the surface. However, at nanoscale the surface states can profoundly influence or completely dominate the electronic properties, affecting for example the conductance and charge transport through nanowires [71]. This can also effect the mechanical strength, heat dissipation, heat flow, etc. The surface plays a significant role in the modern nanotechnology e.g. semiconductor devices or heterogeneous catalysis.

If the surface is of several atomic layers it can be considered as a 2D (two dimensional) surface. This 2D surface is enormously studied as a part of 2D surface crystallography [72,73]. 2D materials like graphene, borophene, germanene, silicene, phosphorene, antimonene, and bismuthene, plumbene etc. find enormous application areas due to their extraordinary properties and applicability in various ways [74–87]. The realization of the last element of group 14, plumbene have been elusive until Yuhara et al [88] have characterized the successful growth on Pd(111). Typically, very recently, molecular dynamics simulations revealed that the mechanical properties of plumbene are several times greater than those of bulk lead [89].

A lot of studies have been conducted for the production of plumbene and a profound suggestion has come out that Pd (111) could be the substrate where plumbene can be grown. Pb should be adsorbed on a Pd (111) substrate to grow plumbene using segregation technique. Low energy electron diffraction technique gives us the opportunity to characterize the surface with vast information. The energy range of less than 1000 eV which is suitable for its low penetration depth and wavelength of around 1 Å gives the atomic resolution to get the details of the surface structure. The determination of this structure with the numerical values makes it more reliable technique to the experimentalists as well as theorists.

In this experiment, at first we have cleaned the Pd(111) which is confirmed using Auger electron spectroscopy (AES) and then determined the surface relaxation using low energy electron diffraction (LEED). The surface relaxation obtained in our experiment is different compared to the previous report by Ohtani et al [90]. However, the Pendry reliability factor in our case is lower compared and the discrepancy may arise due to the presence of foreign materials in previous experiment. The structure determination of Pd(111) finds immense importance on the context of growing plumbene on it.

3.2 INSTRUMENTATION

The Pd (111) sample was clamped by tantalum plates on molybdenum blocks insulated by an aluminium nitrate sheet for resistive heating in an UHV chamber. The sample holder then mounted at the end of the tube which was then cooled down by introducing liquid N_2

into the tube. LEED and AES optics was available in the chamber which works better in the pressure higher than 1x10^{-8} Pa. They were surrounded with magnetic shields. The temperature was measured using thermo-spot sensor (FTZ6, Japan sensor). For the sample cleaning process, cycling of argon sputtering and annealing at high temperature (800 ^{0}C) was used in Ultra High Vacuum condition. The obtained surface as studied by LEED I(E) in the chamber, without replacing the sample. A movable shutter was deployed to protect the LEED screen from the damage and contamination during the sputtering and sample annealing. The whole setup is shown in Figure 3.1. Brief descriptions of the corresponding tools are given in the following section.

3.2.1. Ultra High Vacuum Chamber

Vacuum chamber was used here which can create an enclosed environment having 1x10^{-8} Pa pressure. This was possible by using four different pumps. They are - rotary pump, sublimation pump, ion pump and turbo molecular pump.

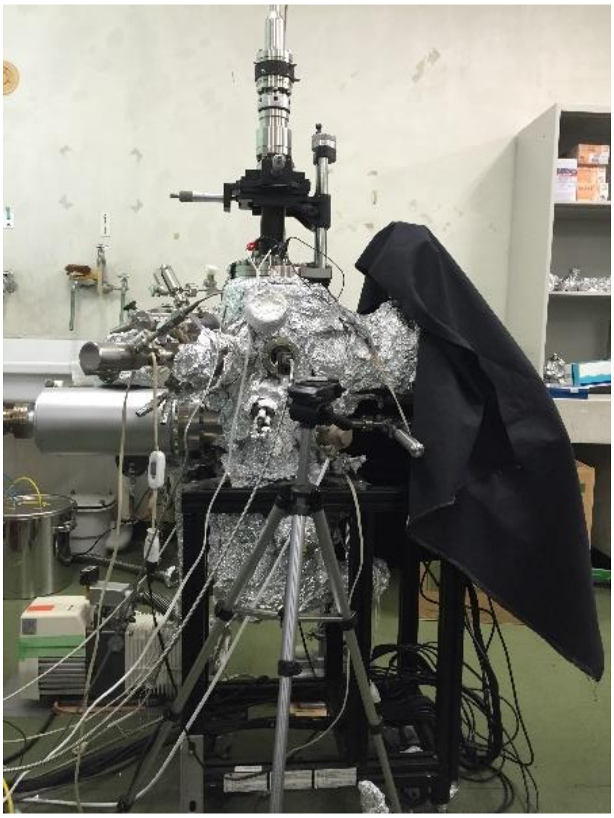

Figure 3.1 *Experimental setup (UHV part)*

3.2.1.1 Rotary-vane pump:

Rotary-vane pumps are a common type of vacuum pump, with two-stage pumps able to reach pressures well below 10^{-6} bar. Main part of this pump is the rotor which turns and corresponding gas flows into the enlarging suction chamber until the second valve seals off the chamber. If the outlet valve is not open by the atmospheric pressure the gas is remain compressed.

3.2.1.2 Sublimation pump

The sublimation pump is a vacuum pump that is used as a part of vacuum systems so that the level of vacuum improves. Here, a high constant current is used through titanium filament which causes the sublimation. The sublimated titanium can get deposited on the chamber walls. Some gases then trapped on the titanium atom, hence pressure is reduced [91].

3.2.1.3 Ion pump

Ion pumps are electro-physical vacuum pumps that remove gases from their environment by turning them into solid materials. It works in four steps: a) creates high magnetic field, b) generates plasma, c) ionize gas molecules d) capture gas ions.

3.2.1.4 Turbo molecular pump

Molecules are adsorbed in the blades of the pump and leave again after certain period of time, where the speed of blade is higher than the thermal molecular speed to ensure that the transferred molecules are not able to come back to the chamber [92].

3.2.2 Manipulator

A manipulator was employed in the UHV chamber to allow the 3D movement of the sample. It is also used for fine tuning of the electron beam normalization by adjustment of the limited inclination of the rod with respect to the vertical axis. The sample was annealed by direct current passing through the sample via the Ta wires from a DC power supply. During annealing the temperature of the samples were measured by infrared pyrometer and thermocouple.

3.2.3 Sources

Several gas or liquid sources were attached through variable leak valve to the UHV chamber. Solid sources such as Silicon, Lead, Germanium, Bismuth and Tin were put in a Ta tube with small hole, and they were evaporated by heating of the ta tube and come out from the small hole to the sample surface.

3.2.4 Thermo-sensor

Radiation pyrometer was used to measure the temperature of the sample surface which have temperature sensing range of 600-2000^{o}C.

3.2.5 Low Energy Electron Diffraction (LEED)

LEED images were used to analyse the clean Pd surface structure. LEED spot intensities were measured using a digital charge-coupled device (CCD) camera with computer controlled data acquisition system [93]. A brief description of LEED optics is presented below:

The LEED measurements were performed in an ultra-high vacuum (UHV) chamber. The chamber was equipped with a four-grid commercial OMICRON LEED optics. In our experiment the base pressure in the chamber was 1×10^{-8} Pa.

The Commercial Omicron SPECTALEED four grid LEED-AES optics was installed in the chamber. A monochromatic electron beam (20-500 eV), was generated by the electron gun, to incident upon a sample[94]. After undergoing diffraction, the electrons were backscattered from the periodic surface and travel through a series of grids, as shown in Figure 3.2. The outer grid, which was placed nearest to the sample, is grounded to ensure that the electrons travel in a field free region, as the inner grid and the sample are grounded. The inner grids were used to filter the electrons, and the elastically scattered electrons can be reached to a fluorescent screen. A digital CCD camera was fixed at the backside viewpoint to acquire the LEED patterns (Figure 3.3).

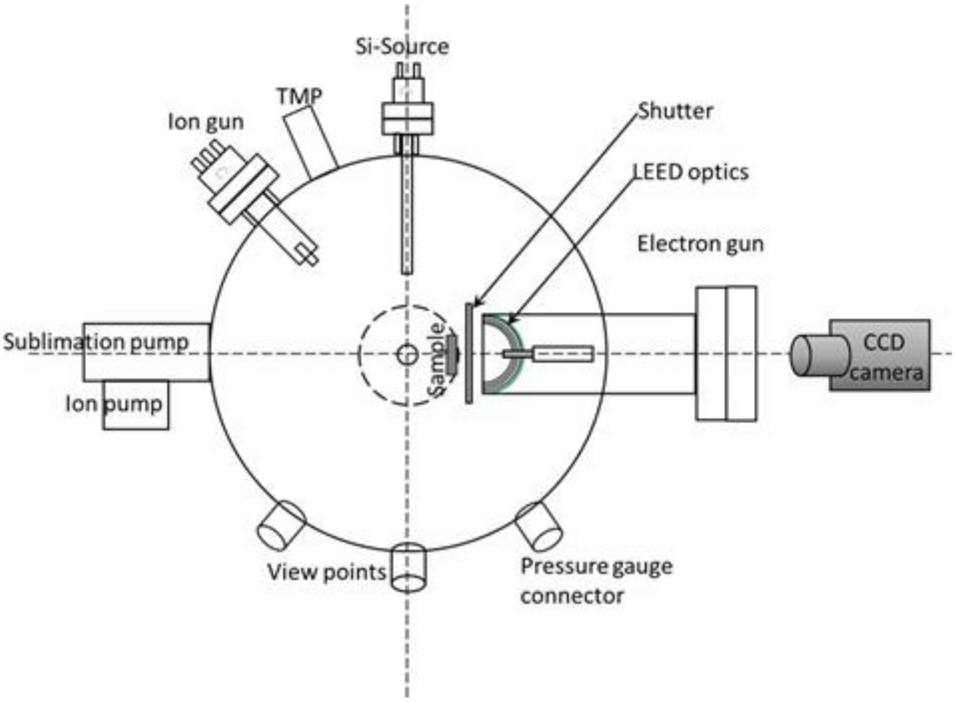

Figure 3.2 Schematic diagram of LEED-AES UHV chamber

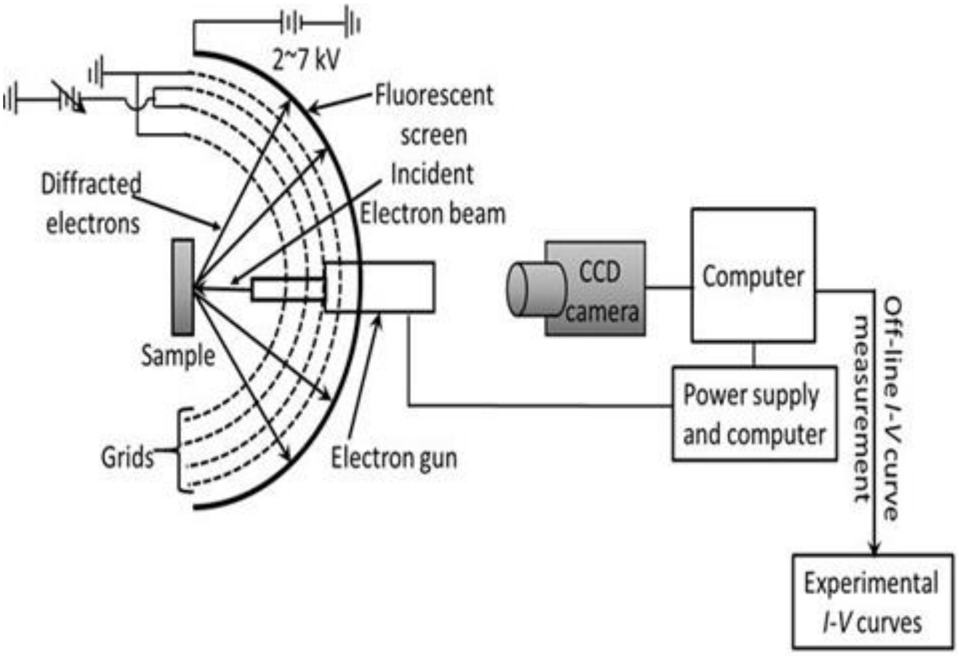

Figure 3.3 Computer controlled data acquisition LEED system

3.3 EXPERIMENT

There are several steps involved in determining the surface structure of clean Pd (111). At first, the chamber needs to be prepared. The vacuum condition of the order 10^{-8} Pa is achieved using rotary vane, sublimation, ion and turbo molecular pumps. The chamber was also baked for several hours prior to this to have an even better vacuum condition. After getting the desired vacuum condition inside chamber the sample was cleaned using argon sputtering and annealing. High energy argon ions were first bombarded towards the exposed surface of Pd (111) substrate. The argon ions etched out 1 or 2 atomic layers of Pd substrate. These layers also included the surface impurities. After the impurities etched out a pure but non smooth layer of Pd surface left. Then the substrate was annealed at 800 k to obtain a smooth layer at the surface. When heated the atoms would migrate and upon cooling down they would be much more relaxed to a make a smooth surface. After that the LEED pattern was observed and I(E) curves were obtained using the intensities of LEED spots.

The Barbieri/Van Hove symmetrized automated-tensor LEED package was used to calculate the theoretical I(E) curves of the structure models to determine the atomic positions [95]. The calculations of atomic scattering were performed by considering 13 phase shifts (lmax = 12), whereas the imaginary part of the inner potential (Voi) was fixed at −5.0 eV and the real part was determined through theoretical-experimental matching and attributed by minimizing Pendry’s reliability factor (Rp). The error bars on the structural parameters were calculated from the variance of Rp, $\Delta R = R_{min}(8|Voi|/\Delta E)1/2$, where R_{min} is the minimum Rp value and ΔE is the total energy range of the experimental I(E) curve.

3.4 RESULTS AND DISCUSSION

3.4.1 Auger electron spectroscopy

The auger electron spectroscopy (AES) of the clean surface is shown in Figure 3.4 the spectra shows the main peak of palladium at 330 eV and other palladium related peaks. This confirms that there are no other foreign elements expect Pd atoms on the surface of the substrate.

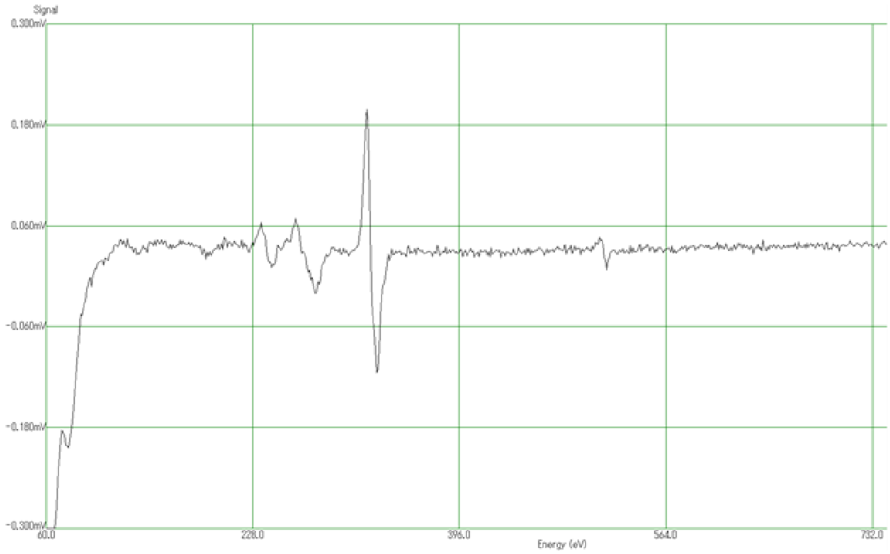

Figure 3.4 Auger electron spectroscopy of clean surface showing the peak corresponding Pd atoms.

3.4.2 LEED pattern analysis

The LEED pattern of the clean Pd(111) surface in shown in Fig 3.5 at (a) 120 eV and (b) 270 eV which were recorded at low temperature of 120 K. The Pd(111) surface shows a 3-fold rotational symmetry from which intensity of five symmetrically independent beams were collected for experimental calculation.

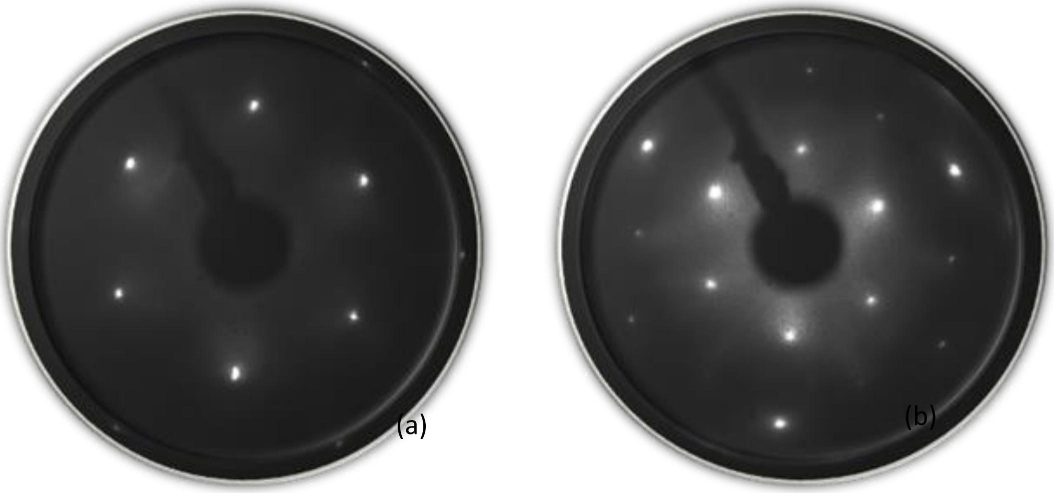

Figure 3.5 Figure 1LEED pattern of clean Pd(111) at (a)120 eV and (b) 270 eV

3.4.3 I-V curve analysis

The comparison between the best fit experimental and theoretical curve is shown in Figur3.6. For five beams: (1,0), (0,1), (1,1), (2,0) and (0,2). The optimized structure has Debye temperatures of 140 K, 220 k and 280 K for first, second and third Pd layer respectively. The optimized structure yields a Pendry Rp factor of 0.14.

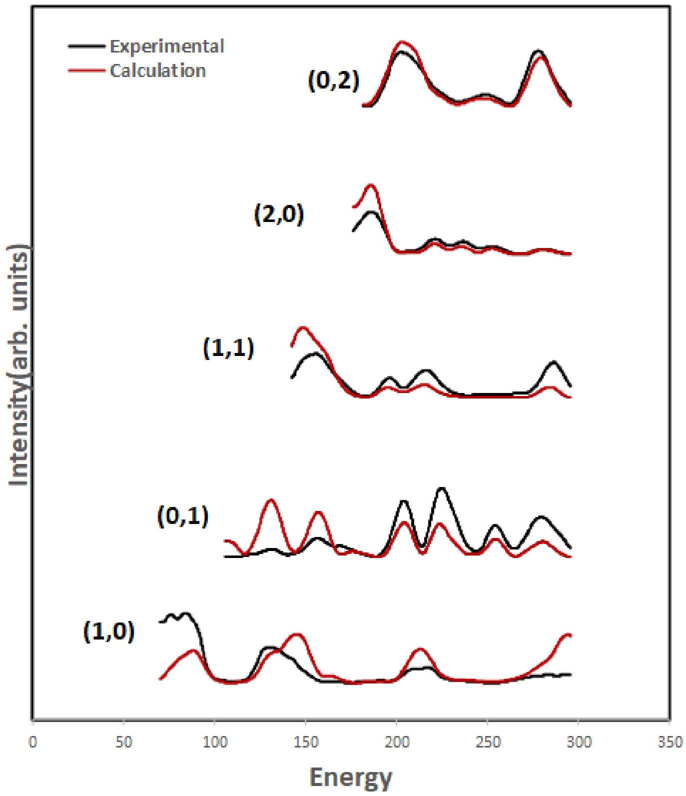

Figure 3.6 Best fit comparison between the theoretical and experimental I(E) curves having Pendry reliability factor Rp = 0.14.

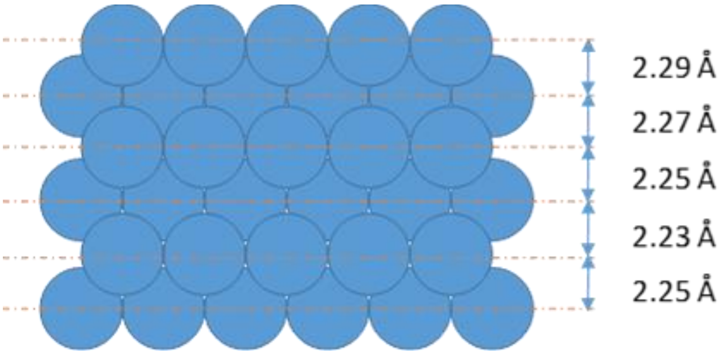

Figure 3.7 Ball model of the surface relaxation of clean Pd(111)

The sphere ball model of the relaxed structure is shown in Figure 3.7 the relaxation sequence for the first six layers are (+; +; +; -; +; +) compared to the bulk termination of 2.24 Å.

3.5 CONCLUSION

In summary, the clean Pd(111) surface structure is determined using LEED analysis. AES spectra confirmed the cleanliness of the surface after which the relaxation of the Pd(111) surface is determined. The relaxation sequence shows (+; +; +; -; +; +) which shows discrepancy with the previous data. However, our reliability factor is much lower compared to the published data and this can give important information for further studies regarding growth of 2D materials.

Acknowledgement:

I would like to express my heart felt gratitude towards doctoral student ***Mr. Rezwan Ahmed*** to guide me learning this LEED technique and also helping me in various ways to complete this lab rotation.

General Conclusion

The overall conclusion of this thesis is summarized as follows:

- Some potential adsorbent/refrigerant pairs are studied in terms of their thermodynamic compatibility in designing an adsorption cooling system. These pairs are compared in terms of their isosteric heat, enthalpy and entropy. In case of isosteric heat ACF-A20/R32, Maxsorb III/R134a and Maxsorb III/R32 pairs were found suitable for cooling application. However, ACF-A-20/R134a and Maxsorb III/n butane pairs could be the pairs for designing a heating system. When considering enthalpy ACF-A-20/R32 pair shows best characteristics to be the pair for chosen in case of cooling application. And if entropy is given the priority in choosing best pair cooling applications ACF-A20/R134a or Maxsorb III/ R32 pair stands out depending on the cooling load required. Another fact found here was the effect of fluorine atoms in isosteric heat of adsorption. The more fluorine atoms present in the refrigerant the lesser the variation in isosteric heat of adsorption before being positive when there were 6 atoms in case of $SF_{6.}$ Also T-s mapping was done for different cooling conditions for all the discussed pairs. All of them showed positive response when the cooling load was reduced. But in case of ACF-A-20/R134a pair the improvement was the highest.
- Aluminum fumarate metal organic framework is successfully synthesized using a green synthesis technique involving the hydro-thermal procedures. The XRD and FESEM characterizations is performed for this sample and matched with published literature to confirm its authenticity of being aluminum fumarate. The porous properties and water adsorption properties are measured and compared with the data for the commercial aluminum fumarate sample. And the synthesized sample is found to be superior when compared with the commercial aluminum fumarate.
- The clean Pd(111) structure is determined using low energy electron diffraction and auger electron spectroscopy with the relaxations until 6 atomic layers. The relaxation was found to be having a sequence of (+, +, +, -, +, +) with a Pendry's

reliability factor of 0.14. this result contradicts with published result but as the Rp is lower for this case, we can consider our data to be more accurate.

RECOMMENDATIONS

In this section there are some directions given for future researchers to successfully utilize and further extend this study.

- The thermodynamic property field analysis shows that there could be others parameters to be taken care of other that only adsorption uptake and kinetics when designing a practical adsorption system. This open a new scope of study to make sure which parameter should be given highest priority. Or maybe there is scope for optimization.
- The green synthesis of aluminum fumarate technique can be applied to synthesize similar MOFs. Also we can dope different metal nodes or try different linker organic materials. All these can have an effect on the pore size modification, adsorption affinity, kinetics and so on. Also in MOFs isotherms can be shifted and also modified.
- The clean Pd(111) surface structure with surface relaxations can be applied in future 2D material growth (like plumbene) having Pd(111) as substrate.

Reference

[1] L. García, Y.A. Poveda, G. Rodríguez, E. Esche, H.R. Godini, G. Wozny, J.U. Repke, Á. Orjuela, Adsorption separation of oxidative coupling of methane effluent gases. Mini-plant scale experiments and modeling, J. Nat. Gas Sci. Eng. 61 (2019) 106–118. doi:10.1016/j.jngse.2018.11.007.

[2] D.A. Kennedy, M. Mujčin, C. Abou-Zeid, F.H. Tezel, Cation exchange modification of clinoptilolite –thermodynamic effects on adsorption separations of carbon dioxide, methane, and nitrogen, Microporous Mesoporous Mater. 274 (2019) 327–341. doi:10.1016/J.MICROMESO.2018.08.035.

[3] A. Abedini, E. Crabtree, J.E. Bara, C.H. Turner, Molecular analysis of selective gas adsorption within composites of ionic polyimides and ionic liquids as gas separation membranes, Chem. Phys. 516 (2019) 71–83. doi:10.1016/j.chemphys.2018.08.039.

[4] D.G. Pahinkar, S. Garimella, A novel temperature swing adsorption process for natural gas purification: Part I, model development, Sep. Purif. Technol. 203 (2018) 124–142. doi:10.1016/J.SEPPUR.2018.04.020.

[5] S.J. Chen, Y. Fu, Y.X. Huang, Z.C. Tao, M. Zhu, Experimental investigation of CO2 separation by adsorption methods in natural gas purification, Appl. Energy. 179 (2016) 329–337. doi:10.1016/J.APENERGY.2016.06.146.

[6] S. Kayal, S. Baichuan, B.B. Saha, Adsorption characteristics of AQSOA zeolites and water for adsorption chillers, Int. J. Heat Mass Transf. 92 (2016) 1120–1127. doi:10.1016/J.IJHEATMASSTRANSFER.2015.09.060.

[7] M.Z.I. Khan, K.C.A. Alam, B.B. Saha, A. Akisawa, T. Kashiwagi, Performance evaluation of multi-stage, multi-bed adsorption chiller employing re-heat scheme, Renew. Energy. 33 (2008) 88–98. doi:10.1016/j.renene.2007.01.012.

[8] B.B. Saha, I.I. El-Sharkawy, A. Chakraborty, S. Koyama, Study on an activated carbon fiber-ethanol adsorption chiller: Part I - system description and modelling,

Int. J. Refrig. 30 (2007) 86–95. doi:10.1016/j.ijrefrig.2006.08.004.

[9] L.H. Zou, H.M. Liu, L.H. Gong, Cryogenic adsorption of nitrogen on activated carbon: Experiment and modeling, Cryogenics (Guildf). 90 (2018) 20–29. doi:10.1016/j.cryogenics.2018.01.001.

[10] N. Cherrad, Conditioning of hydrogen storage by continuous solar adsorption in activated carbon AX-21 with simultaneous production, Int. J. Hydrogen Energy. 44 (2018) 2153–2163. doi:10.1016/j.ijhydene.2018.05.023.

[11] X. Zhang, Q. Huang, M. Liu, J. Tian, G. Zeng, Z. Li, K. Wang, Q. Zhang, Q. Wan, F. Deng, Y. Wei, Preparation of amine functionalized carbon nanotubes via a bioinspired strategy and their application in Cu2+ removal, Appl. Surf. Sci. 343 (2015) 19–27. doi:10.1016/J.APSUSC.2015.03.081.

[12] Q. Huang, M. Liu, J. Chen, Q. Wan, J. Tian, L. Huang, R. Jiang, Y. Wen, X. Zhang, Y. Wei, Facile preparation of MoS2 based polymer composites via mussel inspired chemistry and their high efficiency for removal of organic dyes, Appl. Surf. Sci. 419 (2017) 35–44. doi:10.1016/J.APSUSC.2017.05.006.

[13] Q. Huang, M. Liu, L. Mao, D. Xu, G. Zeng, H. Huang, R. Jiang, F. Deng, X. Zhang, Y. Wei, Surface functionalized SiO2 nanoparticles with cationic polymers via the combination of mussel inspired chemistry and surface initiated atom transfer radical polymerization: Characterization and enhanced removal of organic dye, J. Colloid Interface Sci. 499 (2017) 170–179. doi:10.1016/J.JCIS.2017.03.102.

[14] X. Zhang, Q. Huang, F. Deng, H. Huang, Q. Wan, M. Liu, Y. Wei, Mussel-inspired fabrication of functional materials and their environmental applications: Progress and prospects, Appl. Mater. Today. 7 (2017) 222–238. doi:10.1016/J.APMT.2017.04.001.

[15] Y. Liu, H. Huang, D. Gan, L. Guo, M. Liu, J. Chen, F. Deng, N. Zhou, X. Zhang, Y. Wei, A facile strategy for preparation of magnetic graphene oxide composites and their potential for environmental adsorption, Ceram. Int. 44 (2018) 18571–

18577. doi:10.1016/J.CERAMINT.2018.07.081.

[16] H.T. Chua, K.C. Ng, A. Chakraborty, N.M. Oo, Thermodynamic property fields of an adsorbate-adsorbent system, Langmuir. 19 (2003) 2254–2259. doi:10.1021/la0267140.

[17] A. Pal, K. Thu, S. Mitra, I.I. El-Sharkawy, B.B. Saha, H.-S. Kil, S.-H. Yoon, J. Miyawaki, Study on biomass derived activated carbons for adsorptive heat pump application, Int. J. Heat Mass Transf. 110 (2017) 7–19. doi:10.1016/J.IJHEATMASSTRANSFER.2017.02.081.

[18] K.C. Chan, C.Y.H. Chao, C.L. Wu, Measurement of properties and performance prediction of the new MWCNT-embedded zeolite 13X/CaCl2 composite adsorbents, Int. J. Heat Mass Transf. 89 (2015) 308–319. doi:10.1016/J.IJHEATMASSTRANSFER.2015.05.063.

[19] I.I. El-Sharkawy, K. Uddin, T. Miyazaki, B.B. Saha, S. Koyama, J. Miyawaki, S.-H. Yoon, Adsorption of ethanol onto parent and surface treated activated carbon powders, Int. J. Heat Mass Transf. 73 (2014) 445–455. doi:10.1016/J.IJHEATMASSTRANSFER.2014.02.046.

[20] M. Sultan, T. Miyazaki, B.B. Saha, S. Koyama, H.-S. Kil, K. Nakabayashi, J. Miyawaki, S.-H. Yoon, Adsorption of Difluoromethane (HFC-32) onto phenol resin based adsorbent: Theory and experiments, Int. J. Heat Mass Transf. 127 (2018) 348–356. doi:10.1016/J.IJHEATMASSTRANSFER.2018.07.097.

[21] K. Uddin, I.I. El-Sharkawy, T. Miyazaki, B.B. Saha, S. Koyama, H.S. Kil, J. Miyawaki, S.H. Yoon, Adsorption characteristics of ethanol onto functional activated carbons with controlled oxygen content, Appl. Therm. Eng. 72 (2014) 211–218. doi:10.1016/j.applthermaleng.2014.03.062.

[22] B.B. Saha, I.I. El-Sharkawy, R. Thorpe, R.E. Critoph, Accurate adsorption isotherms of R134a onto activated carbons for cooling and freezing applications, Int. J. Refrig. 35 (2012) 499–505. doi:10.1016/j.ijrefrig.2011.05.002.

[23] A. Pal, A. Kondor, S. Mitra, K. Thu, S. Harish, B.B. Saha, On surface energy and acid–base properties of highly porous parent and surface treated activated carbons using inverse gas chromatography, J. Ind. Eng. Chem. 69 (2018) 432–443. doi:10.1016/j.jiec.2018.09.046.

[24] A. Pal, I.I. El-Sharkawy, B.B. Saha, S. Jribi, T. Miyazaki, S. Koyama, Experimental investigation of CO2 adsorption onto a carbon based consolidated composite adsorbent for adsorption cooling application, Appl. Therm. Eng. 109 (2016) 304–311. doi:10.1016/J.APPLTHERMALENG.2016.08.031.

[25] A. Chakraborty, B.B. Saha, S. Koyama, K.C. Ng, On the thermodynamic modeling of the isosteric heat of adsorption and comparison with experiments, Appl. Phys. Lett. 89 (2006) 171901. doi:10.1063/1.2360925.

[26] S. Jribi, A. Chakraborty, I.I. El-Sharkawy, B.B. Saha, S. Koyama, Thermodynamic Analysis of Activated Carbon-CO2 based Adsorption Cooling Cycles, World Acad. Sci. Eng. Technol. 2 (2008) 63–66.

[27] B.B. Saha, A. Chakraborty, S. Koyama, S.H. Yoon, I. Mochida, M. Kumja, C. Yap, K.C. Ng, Isotherms and thermodynamics for the adsorption of n-butane on pitch based activated carbon, Int. J. Heat Mass Transf. 51 (2008) 1582–1589. doi:10.1016/j.ijheatmasstransfer.2007.07.031.

[28] V.K. Singh, E.A. Kumar, Experimental investigation and thermodynamic analysis of CO2adsorption on activated carbons for cooling system, J. CO2 Util. 17 (2017) 290–304. doi:10.1016/j.jcou.2016.12.004.

[29] K. Uddin, M. Amirul Islam, S. Mitra, J. Lee, K. Thu, B.B. Saha, S. Koyama, Specific heat capacities of carbon-based adsorbents for adsorption heat pump application, Appl. Therm. Eng. 129 (2018) 117–126. doi:10.1016/j.applthermaleng.2017.09.057.

[30] K. THU, N. TAKEDA, T. MIYAZAKI, B.B. SAHA, S. KOYAMA, T. MARUYAMA, S. MAEDA, T. KAWAMATA, Experimental investigation on the

performance of an adsorption system using Maxsorb III + ethanol pair, Int. J. Refrig. (2018). doi:10.1016/j.ijrefrig.2018.06.009.

[31] M. Kumita, N. Yamawaki, K. Shinohara, H. Higashi, A. Kodama, N. Kobayashi, T. Seto, Y. Otani, Methanol adsorption behaviors of compression-molded activated carbon fiber with PTFE, Int. J. Refrig. 94 (2018) 127–135. doi:10.1016/j.ijrefrig.2018.07.036.

[32] B.B. Saha, K. Habib, I.I. El-Sharkawy, S. Koyama, Adsorption characteristics and heat of adsorption measurements of R-134a on activated carbon, Int. J. Refrig. 32 (2009) 1563–1569. doi:10.1016/j.ijrefrig.2009.03.010.

[33] J.M. Calm, The next generation of refrigerants – Historical review, considerations, and outlook, Int. J. Refrig. 31 (2008) 1123–1133. doi:10.1016/J.IJREFRIG.2008.01.013.

[34] United Nations, Montreal protocol on substances that deplete the ozone layer. Montreal, 16 September 1987., Montreal, 1987. https://treaties.un.org/doc/Treaties/1989/01/19890101 03-25 AM/Ch_XXVII_02_ap.pdf.

[35] Kyoto Protocol to the United Nations Framework Convention on Climate Change, Rev. Eur. Community Int. Environ. Law. 7 (1998) 214–217. doi:10.1111/1467-9388.00150.

[36] The Copenhagen Amendment (1992): The amendment to the Montreal Protocol agreed by the Fourth Meeting of the Parties (Copenhagen, 23-25 November 1992) | Ozone Secretariat, (n.d.). https://ozone.unep.org/en/handbook-montreal-protocol-substances-deplete-ozone-layer/2199 (accessed April 16, 2019).

[37] G.A. Longo, S. Mancin, G. Righetti, C. Zilio, Saturated vapour condensation of R410A inside a 4 mm ID horizontal smooth tube: Comparison with the low GWP substitute R32, Int. J. Heat Mass Transf. 125 (2018) 702–709. doi:10.1016/J.IJHEATMASSTRANSFER.2018.04.109.

[38] Z. Meng, H. Zhang, M. Lei, Y. Qin, J. Qiu, Performance of low GWP R1234yf/R134a mixture as a replacement for R134a in automotive air conditioning systems, Int. J. Heat Mass Transf. 116 (2018) 362–370. doi:10.1016/J.IJHEATMASSTRANSFER.2017.09.049.

[39] L. Lin, M.A. Kedzierski, Review of low-GWP refrigerant pool boiling heat transfer on enhanced surfaces, Int. J. Heat Mass Transf. 131 (2019) 1279–1303. doi:10.1016/J.IJHEATMASSTRANSFER.2018.11.142.

[40] Q. Guo, M. Li, H. Gu, Condensation heat transfer characteristics of low-GWP refrigerants in a smooth horizontal mini tube, Int. J. Heat Mass Transf. 126 (2018) 26–38. doi:10.1016/J.IJHEATMASSTRANSFER.2018.05.034.

[41] A. López-Belchí, F. Illán-Gómez, Evaluation of a condenser based on mini-channels technology working with R410A and R32. Experimental data and performance estimate, Appl. Energy. 202 (2017) 112–124. doi:10.1016/J.APENERGY.2017.05.122.

[42] G. Chen, V. Ierin, O. Volovyk, K. Shestopalov, An improved cascade mechanical compression–ejector cooling cycle, Energy. 170 (2019) 459–470. doi:10.1016/J.ENERGY.2018.12.107.

[43] D.R. Dorman, M.L. Timm, G.A. Scrivener, J. Caylor, P.L. Doppel, S.W. Duda, D.M. Halel, P.A. Johnson, J.A. Kohler, C.D. Kolandayan, E.M. Smith, R.P. Vallort, W.F. Walter, R.L. Hall, J.R. Anderson, C.S. Barnaby, S.F. Bruning, J.A. Clark, W.S. Clements, J.M. Ferguson, Safety Standard for Refrigeration Systems, 2014.

[44] M.A. Islam, K. Srinivasan, K. Thu, B.B. Saha, Assessment of total equivalent warming impact (TEWI) of supermarket refrigeration systems, Int. J. Hydrogen Energy. 42 (2017) 26973–26983. doi:10.1016/J.IJHYDENE.2017.07.035.

[45] A.A. Askalany, B.B. Saha, K. Uddin, T. Miyzaki, S. Koyama, K. Srinivasan, I.M. Ismail, Adsorption isotherms and heat of adsorption of difluoromethane on activated carbons, J. Chem. Eng. Data. 58 (2013) 2828–2834.

doi:10.1021/je4005678.

[46] I.I. El-Sharkawy, B.B. Saha, S. Koyama, K.C. Ng, A study on the kinetics of ethanol-activated carbon fiber: Theory and experiments, Int. J. Heat Mass Transf. 49 (2006) 3104–3110. doi:10.1016/J.IJHEATMASSTRANSFER.2006.02.029.

[47] A. Chakraborty, B.B. Saha, K.C. Ng, S. Koyama, K. Srinivasan, Theoretical insight of physical adsorption for a single-component adsorbent + adsorbate system: I. thermodynamic property surfaces, Langmuir. (2009). doi:10.1021/la803289p.

[48] A. Chakraborty, B.B. Saha, K.C. Ng, I.I. El-Sharkawy, S. Koyama, Thermodynamic property surfaces for adsorption of R507A, R134a, and n-butane on pitch-based carbonaceous porous materials, Heat Transf. Eng. (2010). doi:10.1080/01457631003604152.

[49] A. Chakraborty, B.B. Saha, S. Koyama, K.C. Ng, Specific heat capacity of a single component adsorbent-adsorbate system, Appl. Phys. Lett. 90 (2007). doi:10.1063/1.2731438.

[50] J.A. Dunne, M. Rao, S. Sircar, R.J. Gorte, A.L. Myers, Calorimetric Heats of Adsorption and Adsorption Isotherms. 2. O 2 , N 2 , Ar, CO 2 , CH 4 , C 2 H 6 , and SF 6 on NaX, H-ZSM-5, and Na-ZSM-5 Zeolites, Langmuir. 12 (1996) 5896–5904. doi:10.1021/la960496r.

[51] N. Stock, S. Biswas, Synthesis of Metal-Organic Frameworks (MOFs): Routes to Various MOF Topologies, Morphologies, and Composites, Chem. Rev. 112 (2012) 933–969. doi:10.1021/cr200304e.

[52] F.A. Almeida Paz, J. Klinowski, S.M.F. Vilela, J.P.C. Tomé, J.A.S. Cavaleiro, J. Rocha, Ligand design for functional metal–organic frameworks, Chem. Soc. Rev. 41 (2012) 1088–1110. doi:10.1039/C1CS15055C.

[53] G. Maurin, C. Serre, A. Cooper, G. Férey, The new age of MOFs and of their porous-related solids, Chem. Soc. Rev. 46 (2017) 3104–3107. doi:10.1039/C7CS90049J.

[54] Y.B. Huang, J. Liang, X.S. Wang, R. Cao, Multifunctional metal-organic framework catalysts: Synergistic catalysis and tandem reactions, Chem. Soc. Rev. 46 (2017) 126–157. doi:10.1039/c6cs00250a.

[55] Y. Zhang, X. Yang, H.-C. Zhou, Synthesis of MOFs for heterogeneous catalysis via linker design, Polyhedron. 154 (2018) 189–201. doi:10.1016/J.POLY.2018.07.021.

[56] N. Tien-Binh, H. Vinh-Thang, X.Y. Chen, D. Rodrigue, S. Kaliaguine, Crosslinked MOF-polymer to enhance gas separation of mixed matrix membranes, J. Memb. Sci. 520 (2016) 941–950. doi:10.1016/J.MEMSCI.2016.08.045.

[57] Y. Gurdal, S. Keskin, A new approach for predicting gas separation performances of MOF membranes, J. Memb. Sci. 519 (2016) 45–54. doi:10.1016/J.MEMSCI.2016.07.039.

[58] N.A.A. Qasem, R. Ben-Mansour, M.A. Habib, An efficient CO2 adsorptive storage using MOF-5 and MOF-177, Appl. Energy. 210 (2018) 317–326. doi:10.1016/J.APENERGY.2017.11.011.

[59] B. Li, H.-M. Wen, Y. Yu, Y. Cui, W. Zhou, B. Chen, G. Qian, Nanospace within metal–organic frameworks for gas storage and separation, Mater. Today Nano. 2 (2018) 21–49. doi:10.1016/J.MTNANO.2018.09.003.

[60] X.-F. Wang, X.-Z. Song, K.-M. Sun, L. Cheng, W. Ma, MOFs-derived porous nanomaterials for gas sensing, Polyhedron. 152 (2018) 155–163. doi:10.1016/J.POLY.2018.06.037.

[61] M.F. de Lange, K.J.F.M. Verouden, T.J.H. Vlugt, J. Gascon, F. Kapteijn, Adsorption-Driven Heat Pumps: The Potential of Metal–Organic Frameworks, Chem. Rev. 115 (2015) 12205–12250. doi:10.1021/acs.chemrev.5b00059.

[62] F. Jeremias, D. Fröhlich, C. Janiak, S.K. Henninger, Water and methanol adsorption on MOFs for cycling heat transformation processes, New J. Chem. 38 (2014) 1846–1852. doi:10.1039/c3nj01556d.

[63] S.K. Henninger, H.A. Habib, C. Janiak, MOFs as Adsorbents for Low Temperature Heating and Cooling Applications, J. Am. Chem. Soc. 131 (2009) 2776–2777. doi:10.1021/ja808444z.

[64] A. Rezk, R. Al-Dadah, S. Mahmoud, A. Elsayed, Experimental investigation of metal organic frameworks characteristics for water adsorption chillers, Proc. Inst. Mech. Eng. Part C J. Mech. Eng. Sci. 227 (2013) 992–1005. doi:10.1177/0954406212456469.

[65] F. Jeremias, A. Khutia, S.K. Henninger, C. Janiak, MIL-100(Al, Fe) as water adsorbents for heat transformation purposes - A promising application, J. Mater. Chem. 22 (2012) 10148–10151. doi:10.1039/c2jm15615f.

[66] J. Canivet, A. Fateeva, Y. Guo, B. Coasne, D. Farrusseng, Water adsorption in MOFs: fundamentals and applications, Chem. Soc. Rev. 43 (2014) 5594–5617. doi:10.1039/C4CS00078A.

[67] F. Jeremias, V. Lozan, S.K. Henninger, C. Janiak, Programming MOFs for water sorption: amino-functionalized MIL-125 and UiO-66 for heat transformation and heat storage applications, Dalt. Trans. 42 (2013) 15967. doi:10.1039/c3dt51471d.

[68] E. Alvarez, N. Guillou, C. Martineau, B. Bueken, B. Van de Voorde, C. Le Guillouzer, P. Fabry, F. Nouar, F. Taulelle, D. de Vos, J.-S. Chang, K.H. Cho, N. Ramsahye, T. Devic, M. Daturi, G. Maurin, C. Serre, The Structure of the Aluminum Fumarate Metal-Organic Framework A520, Angew. Chemie Int. Ed. 54 (2015) 3664–3668. doi:10.1002/anie.201410459.

[69] F. Jeremias, D. Fröhlich, C. Janiak, S.K. Henninger, Advancement of sorption-based heat transformation by a metal coating of highly-stable, hydrophilic aluminium fumarate MOF, RSC Adv. 4 (2014) 24073–24082. doi:10.1039/C4RA03794D.

[70] E. Elsayed, R. AL-Dadah, S. Mahmoud, A. Elsayed, P.A. Anderson, Aluminium fumarate and CPO-27(Ni) MOFs: Characterization and thermodynamic analysis for

adsorption heat pump applications, Appl. Therm. Eng. 99 (2016) 802–812. doi:10.1016/j.applthermaleng.2016.01.129.

[71] M. Müller-rösch, Femtosecond low-energy electron imaging and diffraction using nanotip photoemitters, Freien Universität, 2016. https://pure.mpg.de/rest/items/item_2457360_2/component/file_2460846/content.

[72] P. V. Shinde, M.K. Singh, Synthesis, Characterization, and Properties of Graphene Analogs of 2D Material, Fundam. Sens. Appl. 2D Mater. (2019) 91–143. doi:10.1016/B978-0-08-102577-2.00004-X.

[73] M. Li, Q. Zhang, H. Ruan, X. Wang, Y. Liu, Z. Lu, J. Hai, An in-situ growth approach to 2D MoS2-2D PbS heterojunction composites with improved photocatalytic activity, J. Solid State Chem. 270 (2019) 98–103. doi:10.1016/j.jssc.2018.11.008.

[74] A. Jayakumar, A. Surendranath, M. PV, 2D materials for next generation healthcare applications, Int. J. Pharm. 551 (2018) 309–321. doi:10.1016/J.IJPHARM.2018.09.041.

[75] R. Irshad, K. Tahir, B. Li, Z. Sher, J. Ali, S. Nazir, A revival of 2D materials, phosphorene: Its application as sensors, J. Ind. Eng. Chem. 64 (2018) 60–69. doi:10.1016/J.JIEC.2018.03.010.

[76] F. Reis, G. Li, L. Dudy, M. Bauernfeind, S. Glass, W. Hanke, R. Thomale, J. Schäfer, R. Claessen, Bismuthene on a SiC substrate: A candidate for a high-temperature quantum spin Hall material, Science (80-.). 357 (2017) 287–290. doi:10.1126/science.aai8142.

[77] J.L. Zhang, S. Zhao, C. Han, Z. Wang, S. Zhong, S. Sun, R. Guo, X. Zhou, C.D. Gu, K. Di Yuan, Z. Li, W. Chen, Epitaxial Growth of Single Layer Blue Phosphorus: A New Phase of Two-Dimensional Phosphorus, Nano Lett. 16 (2016) 4903–4908. doi:10.1021/acs.nanolett.6b01459.

[78] B. Feng, J. Zhang, Q. Zhong, W. Li, S. Li, H. Li, P. Cheng, S. Meng, L. Chen, K.

Wu, Experimental realization of two-dimensional boron sheets, Nat. Chem. 8 (2016) 563–568. doi:10.1038/nchem.2491.

[79] X. Wu, Y. Shao, H. Liu, Z. Feng, Y.L. Wang, J.T. Sun, C. Liu, J.O. Wang, Z.L. Liu, S.Y. Zhu, Y.Q. Wang, S.X. Du, Y.G. Shi, K. Ibrahim, H.J. Gao, Epitaxial Growth and Air-Stability of Monolayer Antimonene on PdTe 2, Adv. Mater. 29 (2017). doi:10.1002/adma.201605407.

[80] M. Wang, E.-H. Yang, THz applications of 2D materials: Graphene and beyond, Nano-Structures & Nano-Objects. 15 (2018) 107–113. doi:10.1016/J.NANOSO.2017.08.011.

[81] P. Vogt, P. De Padova, C. Quaresima, J. Avila, E. Frantzeskakis, M.C. Asensio, A. Resta, B. Ealet, G. Le Lay, Silicene: Compelling experimental evidence for graphenelike two-dimensional silicon, Phys. Rev. Lett. 108 (2012) 1–5. doi:10.1103/PhysRevLett.108.155501.

[82] A. Fleurence, R. Friedlein, T. Ozaki, H. Kawai, Y. Wang, Y. Yamada-Takamura, Experimental evidence for epitaxial silicene on diboride thin films, Phys. Rev. Lett. 108 (2012) 1–5. doi:10.1103/PhysRevLett.108.245501.

[83] M.E. Dávila, L. Xian, S. Cahangirov, A. Rubio, G. Le Lay, Germanene: A novel two-dimensional germanium allotrope akin to graphene and silicene, New J. Phys. 16 (2014). doi:10.1088/1367-2630/16/9/095002.

[84] L. Li, S.Z. Lu, J. Pan, Z. Qin, Y.Q. Wang, Y. Wang, G.Y. Cao, S. Du, H.J. Gao, Buckled germanene formation on Pt(111), Adv. Mater. 26 (2014) 4820–4824. doi:10.1002/adma.201400909.

[85] J. Yuhara, H. Shimazu, K. Ito, A. Ohta, M. Araidai, M. Kurosawa, M. Nakatake, G. Le Lay, Germanene Epitaxial Growth by Segregation through Ag(111) Thin Films on Ge(111), ACS Nano. 12 (2018) 11632–11637. doi:10.1021/acsnano.8b07006.

[86] J. Yuhara, Y. Fujii, K. Nishino, N. Isobe, M. Nakatake, L. Xian, A. Rubio, G. Le Lay, Large area planar stanene epitaxially grown on Ag(1 1 1), 2D Mater. 5 (2018).

doi:10.1088/2053-1583/aa9ea0.

[87] F. Zhu, W. Chen, Y. Xu, C. Gao, D. Guan, C. Liu, D. Qian, S.-C. Zhang, J. Jia, Epitaxial growth of two-dimensional stanene, Nat. Mater. 14 (2015) 1020–1025. doi:10.1038/nmat4384.

[88] J. Yuhara, B. He, N. Matsunami, M. Nakatake, G. Le Lay, Graphene's Latest Cousin: Plumbene Epitaxial Growth on a "Nano WaterCube," Adv. Mater. (2019) 1901017. doi:10.1002/adma.201901017.

[89] D.K. Das, J. Sarkar, S.K. Singh, Effect of sample size, temperature and strain velocity on mechanical properties of plumbene by tensile loading along longitudinal direction: A molecular dynamics study, Comput. Mater. Sci. 151 (2018) 196–203. doi:10.1016/J.COMMATSCI.2018.05.006.

[90] H. Ohtani, M. a. van Hove, G. a. Somorjai, LEED Intensity Analysis of the Surface Structures of Pd(111) and of CO asorbed on Pd(111) in a (√3 X √3)R30° Arrangement, Surf. Sci. 187 (1987) 372–386. https://pdf.sciencedirectassets.com/271619/1-s2.0-S0039602887X80012/1-s2.0-S0039602887800638/main.pdf?X-Amz-Security-Token=AgoJb3JpZ2luX2VjEPf%2F%2F%2F%2F%2F%2F%2F%2F%2F%2FwEaCXVzLWVhc3QtMSJHMEUCIH%2FZZJIqaZGivYHbA5f16kLKvwOQ%2FzCpCQ9LPM7Cpjo%2BAiEAhaQ4Em.

[91] R. Cyranski, J. Leck, Pumping characteristics of a vacuum system using a rotary pump and sublimation pump, Vacuum. 26 (1976) 371–375. doi:10.1016/S0042-207X(76)80226-6.

[92] O.B. Malyshev, Characterisation of a turbo-molecular pumps by a minimum of parameters, Vacuum. (2007). doi:10.1016/j.vacuum.2005.11.055.

[93] S. Mizuno, H. Tochihara, A. Barbieri, M.A. Van Hove, Completion of the structural determination of and rationalization of the surface-structure sequence (2×1)→(3×3)→(4×4) formed on Cu(001) with increasing Li coverage, Phys. Rev.

B. 52 (1995) R11658--R11661. doi:10.1103/PhysRevB.52.R11658.

[94] H.A. Sodano, D.J. Inman, G. Park, A Review of Power Harvesting from Vibration using Piezoelectric Materials, 36 (2004) 197–205.

[95] M.A. Van Hove, W. Moritz, H. Over, P.J. Rous, A. Wander, A. Barbieri, N. Materer, U. Starke, G.A. Somorjai, Automated determination of complex surface structures by LEED, Surf. Sci. Rep. 19 (1993) 191–229. doi:10.1016/0167-5729(93)90011-D.

.